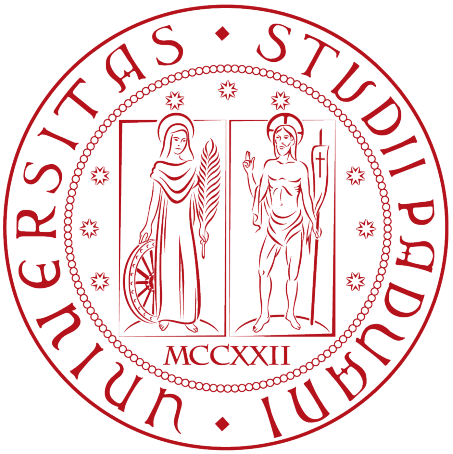

Università degli Studi di Padova

DIPARTIMENTO DI FISICA E ASTRONOMIA "GALILEO GALILEI"
Corso di Laurea in Fisica

Tesi di Laurea Magistrale

Design and optimization around 1 MeV of a Tracker for a CubeSat Mission

Candidato:
Giulio Lucchetta
Matricola 1106625

Relatore:
Dott. Riccardo Rando

Correlatore:
Prof. Denis Bastieri

Anno Accademico 2015-2016

Contents

List of Figures

List of Tables

Abstract

Gamma-ray astrophysics is quite a young field, especially in comparison to the long history of optical observations or even radio-astronomy. Starting with the first observations of telescopes like OSO3 (1967-1969) and SAS2 (1972-1973), in the last two decades many space observatories obtained considerable results: FERMI-LAT (2008-), in the energy range from 20 MeV to 300 GeV, AGILE (2007-), in the energy range from 30 MeV to 50 GeV, COMPTEL (1991-2000), in the energy range from 1 to 30 MeV, and INTEGRAL-IBIS (2002-), in the energy range from 15 keV to 10 MeV, only to name but a few gamma-ray observatories.
At present, the worse sensitivity occurs in the range $1 - 10$ MeV, where the dominant interaction mechanism of gamma rays with matter is Compton scattering. The scientific interest towards this area of the electromagnetic spectrum is actually remarkable. In fact, the MeV regime can provide unique informations about cosmic accelerators, in particular thanks to the detailed study of several emission lines. New data and informations in this range are essential to understand the physical processes powering several cosmic sources like pulsars, supernovae and active galactic nuclei.
For these reasons the next generation of space observatories for gamma-ray astrophysics will focus on the energy range around 1 MeV.

The best instrument to date in this range, COMPTEL onboard CGRO, flew in the 1990's but with a technology dating to a decade earlier. The operating principle of the detector was based on Compton interaction in one of a series of liquid scintillators, and the consecutive absorption in a second plane of NaI scintillators at the distance of 150 cm.
Given the huge leap in technology that occurred since, such as the development of semiconductor detectors and the experience gathered with other gamma-ray observatories like the FERMI-LAT, the performances of a future Compton telescope is expected to improve at least by an order of magnitude with respect to COMPTEL. However, several issues affect this optimistic picture of the situation: the external gamma-ray background produced by the

interaction of charged particles with the atmosphere represents a remarkable complication, the internal background due to material activation produces events in the energy range of signal, and the Compton track reconstruction and event analysis are, generally, quite complex. For these reasons a careful optimization of instrument design and operation is required.

Therefore, the goal of this thesis is a preliminary analysis of the design and the performances of a small Compton detector, with a payload's dimension of $2 - 3$ U, contained development costs and relatively quick design phase. This instrument should be used as a pathfinder for Compton space missions recently proposed (like the ESA mission ASTROGAM and the NASA mission COMPAIR), to be presented again in an updated version in the coming years. The time scale for an M-class mission is around 10 years, with a cost ~ 500 M€, so the realization of a small pathfinder test instrument is of great interest.
The work is focused mainly on the study and optimization of the silicon tracker which will be the heart of a future Telescope optimized in the MeV energy range.

Introduzione

L'astrofisica delle alte energie è un campo relativamente giovane della fisica, specialmente se confrontato con la lunga storia delle osservazioni nell'ottico, o con la radio-astronomia. Partendo dalle prime osservazioni di telescopi come OSO3 (1967-1969) e SAS2 (1972-1973), negli ultimi venti anni numerosi osservatori spaziali hanno ottenuto risultati notevoli: FERMI-LAT (2008-), nel range energetico compreso tra 20 MeV e 300 GeV, AGILE (2007-), nel range compreso tra 30 MeV e 50 GeV, COMPTEL (1991-2000), nel range compreso tra 1 e 30 MeV, ed INTEGRAL-IBIS (2002-), nel range compreso tra 15 keV e 10 MeV, solo per citarne alcuni.
Attualmente la sensitività peggiore è proprio nella finestra $1 - 10$ MeV, dove il meccanismo principale di interazione dei fotoni con la materia è rappresentato dallo scattering Compton. Tuttavia l'interesse scientifico rivolto a questa regione dello spettro elettromagnetico è notevole. Infatti, nel regime del MeV, si possono ottenere prezione informazioni che riguardano gli acceletatori cosmici, in particolare grazie allo studio dettagliato di diverse linee di emissione. Nuovi dati ed informazioni in questo range energetico sono quindi essenziali per comprendere i processi fisici che regolano diverse sorgenti cosmiche come le pulsar, le supernove e i nuclei galattici attivi.

Lo strumento che in passato ha coperto il range intorno ad 1 MeV, COMPTEL, ha iniziato la presa dati negli anni '90 ma fu costruito con una tecnologia sviluppata negli anni '80. Il principio di funzionamento del rivelatore si basava sull'interazione Compton in un primo modulo di scintillatori liquidi, e il successivo assorbimento da parte di un secondo modulo di scintillatori allo Ioduro di Sodio, posti alla distanza di 150 cm rispetto ai primi.
Considerati i grandi passi in avanti compiuti da allora dal punto di vista tecnologico, come lo sviluppo dei rivelatori a semiconduttore, e l'esperienza accumulata attraverso altre missioni spaziali come il FERMI-LAT, è possibile pensare alla realizzazione di un nuovo satellite Compton con delle prestazioni migliori rispetto a quelle di COMPTEL di almeno un ordine di grandezza. Tuttavia, diversi problemi complicano questo quadro ottimistico della situ-

azione: il background esterno di raggi gamma prodotti dall'interazione di particelle cariche con l'atmosfera rappresenta un'enorme fonte di disturbo, il background interno dovuto all'attivazione di materiale passivo produce eventi nel range energetico in esame, e la ricostruzione e l'analisi degli eventi Compton è, generalmente, piuttosto complessa. Per tutti questi motivi è necessaria un'accurata progettazione del satellite e un'attenta ottimizzazione della strumentazione e della procedura di analisi dati.

Pertanto, lo scopo di questa tesi consiste nell'analisi preliminare della progettazione e delle prestazioni di un piccolo satellite Compton, con un payload delle dimensioni di circa $2 - 3$ U, dai costi contenuti e progettabile in tempi relativamente brevi. Questo telescopio potrà essere utilizzato come strumento di test in vista di missioni presentate di recente (come la missione ESA ASTROGAM, e la missione NASA COMPAIR) e che saranno riproposte in versione aggiornata nei prossimi anni. Poiché il time scale per una missione di classe M è di circa 10 anni, con un costo ~ 500 M€, la realizzazione di una piccola sonda pathfinder è di grande interesse.
In particolare il lavoro svolto si è focalizzato principalmente sullo studio e sull'ottimizzazione del tracciatore al silicio, il quale, come vedremo, rappresenta l'elemento fondamentale per un futuro telescopio ottimizzato nel range energetico attorno al MeV.

Chapter 1

Gamma-ray astrophysics in the MeV regime

1.1 Astronomical sources

Gamma-ray astronomy in the MeV regime, from a few hundred keV to several tens of MeV, can provide unique information about the universe. The high penetration power of the gamma rays enables studies of highly obscured sources, and nuclear lines carry information about origin and distribution of individual isotopes in the cosmos, and the underlying processes powering several cosmic sources like supernovae, novae, pulsars etc.
It is not the purpose of this thesis to give a complete and detailed description of all these astronomical sources; in fact in this section are presented only some fundamentals science objectives for a future Compton Telescope. For further information see, for example, [25] and [14].

1.1.1 Supernovae (SNe) and nucleosynthesis

One of the most challenging questions in gamma-ray astronomy is related to type Ia Supernovae.
Supernovae are the brilliant death of a star; these astronomical events can be due to the thermonuclear explosion of a CO white dwarf (SNe Ia) or to the core-collapse of a massive star (SNe II/Ib/Ic). Supernovae have synthesized most of the elements heavier than He, and their light curve is powered, mainly, by the decay $^{56}Ni \rightarrow^{56} Co$ ($t_{1/2} = 6.1\,d$, with a 812 keV line) and $^{56}Co \rightarrow^{56} Fe$ ($t_{1/2} = 77\,d$, with a line at 847 keV). A much smaller contribution is given by ^{57}Co, ^{44}Ti, ^{22}Na and ^{60}Co, as illustrated in Figure 2.8. Evident in the figure is the cascade from the early-time dominance of short-lived radioactivities to the later dominance of long-lived radioactivities. Assuming that a large

fraction of these photons escape, short-lived radioactivities give rise to intense, but brief emission, while long-lived radioactivities give rise to faint, but persistent emission. Moreover, type II Supernovae produce less ^{56}Ni than type Ia Supernovae (the difference of a factor of eight can not be properly identified, since the large scale of the figure), so prompt emission is far fainter in SNe II than SNe Ia.
Initially, the SN density is so large that all X and gamma-ray photons are scattered, but, as the SN expands, the ejecta thins and photons begin to escape. Therefore, the prompt X and gamma-ray line flux from a SN depends upon ejecta mass and kinematics, making the evolution of the fluxes of the various gamma-ray lines a probe of the SN ejecta. In fact, the measurement of the intensity of these lines provides a direct and precise determination of the ^{56}Co mass, which is the main parameter that determines the evolution of optical light curve and relationship between the intensity of the peak and the slope of the post peak.

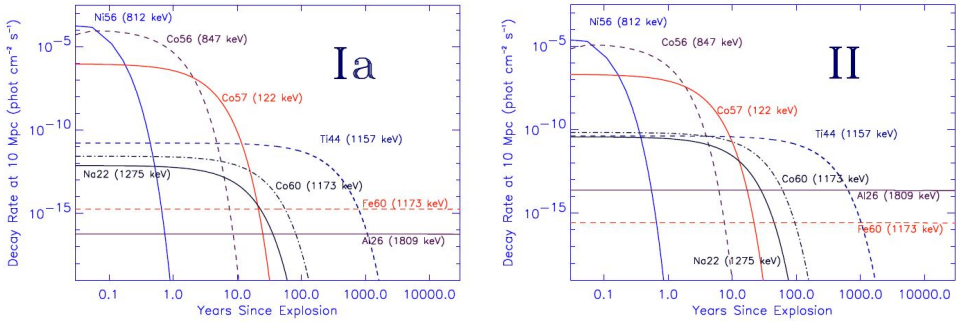

(a) Type Ia Supernova. (b) Type II Supernova.

Figure 1.1: Decay rates of the SN Ia model, W7, and the SN II model, W10HMM; both SNe are assumed at a distance of 10 Mpc (figures taken from [12]).

Although SNe Ia are used as standard candles to measure cosmological distances, many questions about these explosions remain unanswered. Firstly we do not yet know which are the progenitor systems: it is almost certainly that these processes occur in binary systems, but the nature of the companions, whether normal stars or white dwarfs, is still unknown. Moreover, we do not clear understand the propagation processes and several competing models of explosion mechanisms exist: for example, we do not know if the burning front propagates subsonically or supersonically, or a mixture of the two, and to what extent instabilities break spherical symmetry.
The study of gamma-ray line emission in the MeV regime is an excellent

diagnostic of SNe which can contribute to the investigation of explosive nucleosynthesis, as well as radiation transport and galactic chemical evolution. However, since SN rates are on the order of a few SNe per century per galaxy, a Compton Telescope needs a wide Field of view (FoV) and a sensitivity of 10^{-7} photons $\mathrm{cm}^{-2}\,\mathrm{s}^{-1}$, to detect several SNe at the distances on the order of 100 Mpc in a estimate 5 years mission duration.
Moreover the detailed study of other emission lines, like the annihilation line at 511 keV, and the decay lines of nuclear isotopes such as the 1275 keV line from ^{22}Na or the 478 keV line from ^{7}Be, can provide unique information about other cosmic sources like pulsars, novae etc.

1.1.2 Gamma-Ray Bursts (GRBs)

Gamma-ray bursts (GRBs) are extremely energetic explosions that have been observed in distant galaxies; they are one of the brightest electromagnetic events known, to occur in the Universe. These events are associated with massive star explosions or coalescence possibly leading to the formation of black holes. The non-thermal spectra of bursts, that can last from milliseconds to several hours, are commonly interpreted as synchrotron and inverse Compton radiation from electrons accelerated to ultra-relativistic energies in internal shocks. Despite the enormous progress in the study of GRBs, made, for example, by the *Swift* mission (2004-), many aspects concerning the nature of the central engine and the physics of the GRBs emission are still not well understood. A future Compton Telescope, with the possibility of polarization studies will provide new data and contributions to these astronomical events.

1.1.3 Active Galactic Nuclei (AGNs)

Nowadays the most commonly accepted model for Active Galactic Nuclei (AGNs) consists of a rotating super massive black hole, with a mass about 10^6 to 10^9 solar masses, surrounded by an accretion disk and a thick dusty torus. An AGN may be distinguished by the following characteristics:

- a bright nucleus that overcomes the luminosity of the whole host galaxy;
- the presence of broad or narrow emission lines in the optical spectra produced by non-stellar processes;
- jets propagating from the central core, possibly showing superluminal motions;

- continuum non-thermal emission in several wavelength, from radio to gamma-ray band;
- strong variability of the electromagnetic emission, on time scales from hours to years.

In particular blazars are a class of radio-loud active galactic nuclei, comprised of Flat-Spectrum Radio Quasars (FSRQs) and BL Lac objects, and represent the most violent sources of high-energy gamma-ray emission in the known Universe. The observable radiation most likely originates in relativistic jets oriented at a small angle with respect to the line of sight. Their *Spectral Energy Distributions* (SEDs) are characterized by non-thermal continuum spectra with a broad low-frequency component in the radio-UV or X-ray frequency range and a high-frequency component in the range from X-ray to gamma-ray (as it can be seen in Figure 1.2).

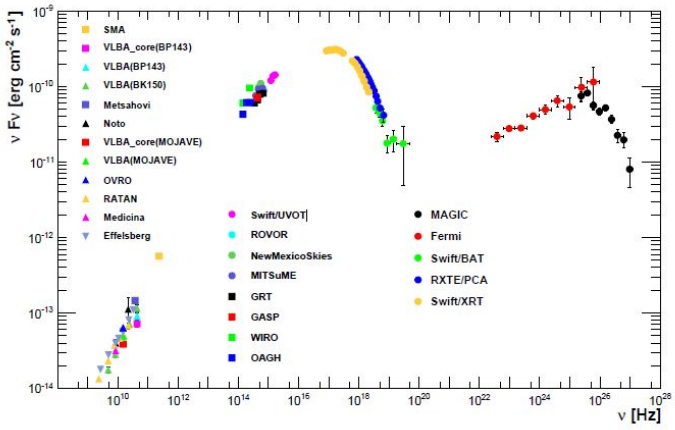

Figure 1.2: Spectral energy distribution of the blazar Mrk 421 averaged over all the observations taken by different telescopes from 2009 January 19, to 2009 June 1 ([4]).

While the origin of the low-frequency (radio through UV or soft X-ray) component of blazar SEDs lies in the synchrotron radiation from, non-thermal, ultrarelativistic electrons, there are two fundamentally different approaches concerning the high-energy emission (X-ray through gamma-ray). If protons are not accelerated to sufficiently high energies to reach the threshold for $p\gamma$ pion production on synchrotron and/or external photons, the high-energy radiation will be dominated by emission from ultrarelativistic electrons and/or pairs (leptonic models). In the opposite case, the high-energy emission will

be dominated by cascades initiated by $p\gamma$ pair and pion production as well as proton, $\pi^{\pm}$, and $\mu^{\pm}$ synchrotron radiation (hadronic models).

- **Leptonic blazar models**. In leptonic models, the radiative output throughout the electromagnetic spectrum is assumed to be dominated by leptons (electrons and positrons). Any protons that are likely present in the outflow, are not accelerated to sufficiently high energies to contribute significantly to the radiative output. The high-energy emission is then most plausibly explained by Compton scattering of low-energy photons by the same electrons producing the synchrotron emission at lower frequencies. Possible target photon fields are the synchrotron photons produced within the jet (the synchrotron self-Compton (SSC) process) or external photons (the external Compton process). Leptonic models, which require the specification of a rather large number of parameters, have met great success in modeling the spectral energy distribution (SEDs) of a large class of blazars. However, the very fast variability of some blazars, poses several problems in the modeling of some sources as, for example, W Comae and 3C 66A (*Böettcher et al., 2013*).

- **Hadronic blazar models**. In hadronic models, both primary electrons and protons are accelerated to ultrarelativistic energies, with protons exceeding the threshold for $p\gamma$ pion production. The acceleration of protons to the necessary ultrarelativistic energies requires high magnetic fields of at least several tens of Gauss. While the low-frequency emission is still dominated by synchrotron emission from primary electrons, the high-energy emission is dominated by proton synchrotron emission, π^0 decay photons, and synchrotron and Compton emission from secondary decay products of charged pions. Hadronic modeling seems problematic in the case of some AGN like 3C 273 and 3C 279 (*Böettcher et al., 2013*).

- **Hybrid blazar models**. The leptonic and hadronic models discussed above are certainly only to be regarded as extreme idealizations of a blazar jet. Realistically, both types of processes should be considered in modeling blazar emission. Nevertheless, for the majority of blazar detected nowadays, we are not able to determine how much is hadronic emission and how much is leptonic emission.

AGNs detection in the energy range around 1 MeV, a widely unexplored region in the electromagnetic spectrum, as it can be seen Figure 1.2 [1], can

[1] roughly 1 MeV corresponds to 10^{22} Hz

provide unique informations in this scenario, determining which component (hadronic or leptonic) is dominant for a given energy in the considered AGN.

1.2 Compton Scattering

Compton scattering, discovered by Arthur Holly Compton in 1922, is the elastic scattering of a photon by an electron. Compton cross-section depends on the atomic number Z of the scatter material; however Compton scattering is the dominant photon-interaction process between $\sim$ 200 keV and $\sim$ 10 MeV, for the majority of materials (Figure 1.3).

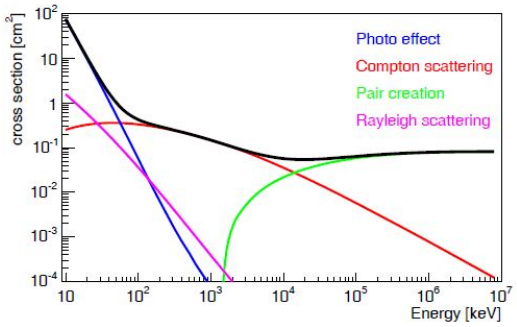

Figure 1.3: Cross-section for the four dominating photon-interaction mechanisms in Silicon ([30]).

The Compton scattering process can be described in terms of energy and momentum conservation of photon and electron:

$$E_i + E_{i,e} = E_g + E_e \tag{1.1}$$

$$\vec{p_i} + \vec{p}_{i,e} = \vec{p_g} + \vec{p_e} \tag{1.2}$$

In general, the initial energy $E_{i,e}$ and momentum $\vec{p}_{i,e}$ of the bound electron are unknown. Assuming that the electron is at rest, the previous equations are modified as follow:

$$E_i + E_0 = E_g + E_e \tag{1.3}$$

$$\vec{p_i} = \vec{p_g} + \vec{p_e} \tag{1.4}$$

where $E_0 = m_e c^2$ is the rest energy of the electron.
From these, the following relation between energies and *Compton scatter angle* can be derived:

$$\cos\varphi = 1 - \frac{E_0}{E_g} + \frac{E_0}{E_g + E_e} \tag{1.5}$$

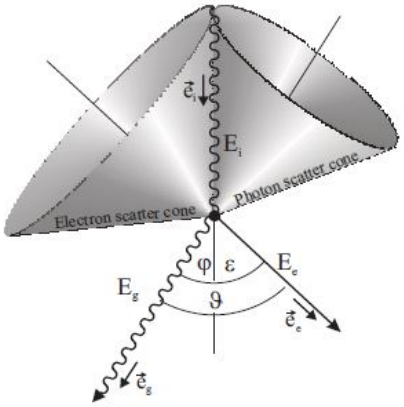

E_i Energy of the incident gamma-ray
E_e Energy of the recoil electron
E_g Energy of the scattered gamma-ray
φ Compton scatter angle of the gamma-ray
ε Scatter angle of the recoil electron
ϑ Total scatter angle
$\vec{e}_i$ Direction of the incident gamma-ray
$\vec{e}_e$ Direction of the recoil electron
$\vec{e}_g$ Direction of the scattered gamma-ray

Figure 1.4: Representation of a Compton-scattering process ([30]).

To get a mathematically valid value for φ (that is, the arccos has the domain $[-1;+1]$), the energy of the recoil electron E_e, and the energy of the scattered gamma ray E_g have the following constrains:

$$\frac{E_0 E_i}{2E_i + E_0} < E_g < E_i \tag{1.6}$$

$$0 < E_e < \frac{2E_i^2}{2E_i + E_0} \tag{1.7}$$

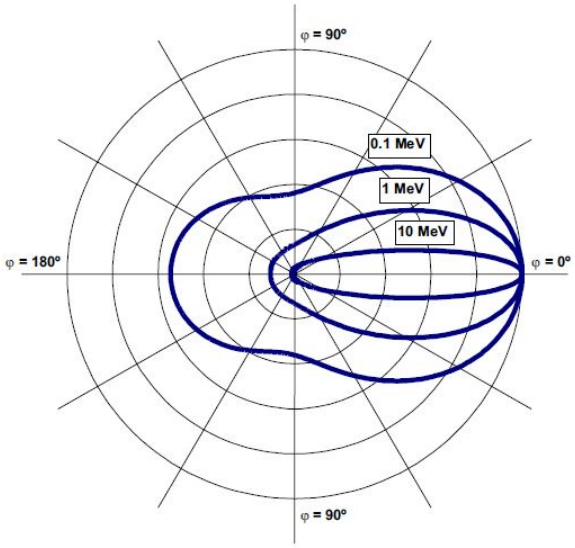

Figure 1.5: Klein-Nishina cross-section as a function of the Compton scatter angle φ for different energies ([30]).

The differential Compton cross-section for unpolarized photons scattering of unbound electrons was derived by Klein and Nishina in 1929:

$$\left(\frac{d\sigma}{d\Omega}\right)_{C,unbound,unpol} = \frac{r_e^2}{2}\left(\frac{E_g}{E_i}\right)^2\left(\frac{E_g}{E_i} + \frac{E_i}{E_g} - \sin^2\varphi\right) \tag{1.8}$$

with r_e classical electron radius.
The forward scattering is favored at higher energies since the average Compton scatter angle is smaller for higher energies, as represented in Figure 1.5. However the Klein-Nishina cross-section constitutes only an approximation, since the electron is assumed not to be bound to an atom and therefore to be at rest.

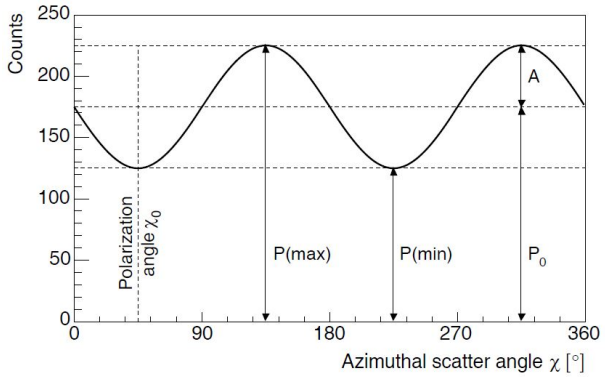

Figure 1.6: Example of a polarization signal for a 100% polarized gamma-ray beam ([30]).

In the case of polarized incident gamma-ray the differential cross-section formula has to be modified in the following:

$$\left(\frac{d\sigma}{d\Omega}\right)_{C,unbound,pol} = \frac{r_e^2}{2}\left(\frac{E_g}{E_i}\right)^2\left(\frac{E_g}{E_i} + \frac{E_i}{E_g} - \sin^2\varphi\cos^2\chi\right) \tag{1.9}$$

where χ is the azimuthal or polar scatter angle.
The probability distribution of the azimuthal scatter angle is:

$$P(\chi) = P_0 + A\cos\left[2\cdot\left(\chi - \chi_0 + \frac{\pi}{2}\right)\right] \tag{1.10}$$

where χ_0 is the direction of the original polarization vector, A is the amplitude and P_0 is the offset of the azimuthal scatter angle distribution.
The polarization response of a detector can be described in terms of the quality factor μ, defined as the ratio between A and P_0:

$$\mu = \frac{P(max) - P(min)}{P(max) + P(min)} = \frac{A}{P_0} \tag{1.11}$$

1.3 Compton Scattering in a real-life Instrument

In the previous section ideal Compton Scattering processes have been studied. However, in any real-life telescope, several additional aspects have to be taken into consideration.
For example if the energies of the recoil electron E_e and the scattered photon E_g, as well as their directions $\vec{e}_e$ and $\vec{e}_g$, are determined with high accuracy, the origin of the photon can be calculated. However, in a real detector these four parameters may not be all measured (or only measured with a large error): in this case it is still possible to constrain the origin of the incident photon.
If the Compton scatter angle is well know, but it is not possible to measure the electron scatter angle, the incident direction of the detected gamma-ray can be restricted to a cone whose opening angle is the Compton scatter angle φ. Otherwise, if the electron scatter angle can be computed, but no information about the photon scatter angle is present, the incident direction of the detected gamma-ray can be restricted to a cone with an opening angle ε.
If no energies are measured or both energies only incompletely, and the electron and the photon scatter directions are well known, photon's origin can partly be retrieved, determining a minimum and maximum possible Compton scatter angle (1.7).

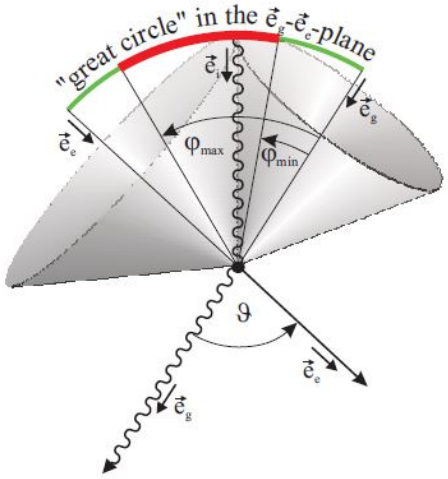

Figure 1.7: Reconstruction of the Compton gamma-ray direction in the case of incomplete measurements (image taken from [30]).

As it can be seen in Figure 1.8, φ_{min} and φ_{max} can be calculated only for some values of the measured gamma-ray and electron energy. If $E_g^{meas} > \frac{E_0}{1-\cos\vartheta}$ and $E_e^{meas} > \frac{2E_0}{\tan^2\vartheta}$, and both values are below/left of the curve, it is possible to determine both φ_{min} and φ_{max}. Otherwise, if $E_g^{meas} < \frac{E_0}{1-\cos\vartheta}$ then no limit on φ_{max} can be determined, while if $E_e^{meas} < \frac{2E_0}{\tan^2\vartheta}$ then no limit on φ_{min} can be given.

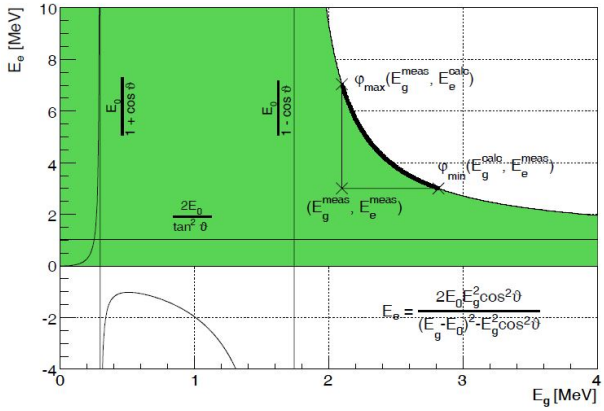

Figure 1.8: Energy of the recoil electron vs. energy of the scattered gamma-ray for a fixed total scatter angle θ ([30]).

The second fundamental aspect to take into account in a real-life detector system, is the fact that electrons are neither free nor at rest, but bound to a nucleus. The unknown momentum of the electron within its atomic energy shell leads to a "Doppler broadening" of the relative energies of the electron and scattered photon, limiting the accuracy with which the incident photon direction can be reconstructed.
To describe this effect, a more sophisticated Compton cross section than the Klein-Nishina equation is required. A suitable expression, that takes into account the momentum distribution of the bound electrons, has been derived by *Ribberfors* (1975):

$$\left(\frac{d\sigma}{d\Omega}\right)_{C,bound,i} = \left(\frac{d\sigma}{d\Omega}\right)_{C,unbound} S_i^I(E_i, \varphi, Z) \tag{1.12}$$

Where Z is the atomic number of the scattering material an S_i^I is called the incoherent scattering function of the i-th shell electrons in the momentum approximation. The expression for S_i^I has been calculated by *Ritterfors and Berggren* (1982).

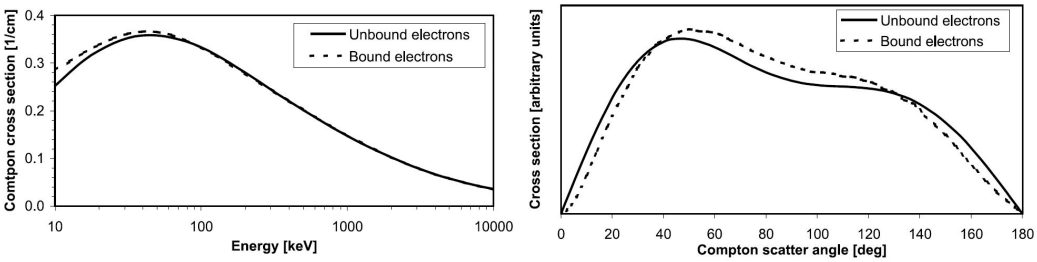

Figure 1.9: Compton cross section for unbound and bound Compton scattering in Silicon, as a function of incident gamma-ray energy (left), and Compton scatter angle at 100 keV (right). The pictures are taken from [30]

The differences between Ribberfors and Klein-Nishina cross sections are illustrated in Figure 1.9. Especially at lower energies, photons have a slightly higher probability to scatter than predicted by the Klein-Nishina equation. Moreover, also the scatter angle distribution changes: in the case of bound electrons small and large scatter angles are suppressed, while the scatter probability increases in the range between $\sim 40°$ and $\sim 130°$.

1.4 Angular resolution for Compton events

For Compton reconstructed events in a real-life telescope the angular resolution can be describe in terms of two different quantities: the *Angular Resolution Measure* or ARM, and the *Scatter Plane Deviation* or SPD.
The ARM is defined as the difference between the computed scatter angle φ, and the true scatter angle φ_{geo}:

$$ARM = \varphi - \varphi_{geo} \tag{1.13}$$

In the ideal case with no measurement errors, ARM will be zero. However in a real-life instrument, energies and locations are measured with a certain error, producing a finite width in the ARM measurement distributed about zero. Therefore the width of the ARM distribution is a measure of the uncertainty in the opening angle of the Compton cone for each reconstructed event.
Instead, the SPD represents the angle between the true scatter plane described by the direction of the incident photon $\vec{e}_i$, and the direction of the scattered photon $\vec{e}_g$, and the measured one spanned by $\vec{e}_g$ and $\vec{e}_e$ (direction of the recoil electron), assuming that $\vec{e}_g$ has been measured correctly:

$$SPD = \arccos((\vec{e}_g \times \vec{e}_i) \circ (\vec{e}_g \times \vec{e}_e)) \tag{1.14}$$

Thus the SPD is relevant only if a measure of $\vec{e}_e$ exist, that is only for tracked events. More intuitively the scatter plane deviation describe the length of the Compton arcs (see, for example, Figure 2.1).

Chapter 2

Compton Telescopes

2.1 Operating principle

The key objective for a Compton Telescope is to determine the direction of motion of the scattered gamma-ray and/or the recoil electron. As illustrated in 2.1, two different types of instrument can fulfill this scope.
In the first type telescopes ("COMPTEL type" telescopes) we have two detector systems: a low-Z scatterer and a high-Z absorber. In the low-Z detector the initial Compton interaction takes place. In the high-Z detector the scattered gamma-ray is absorbed and measured. The two detectors are well separated, so that the time-of-flight of the scattered photon between the two detectors can be measured. Thus top-to-bottom events can be distinguished from bottom-to-top events. With a COMPTEL type instrument it is not possible to measure the direction of the recoil electron, so an ambiguity in the reconstruction of the origin of original photon emerges: the origin can only be reconstructed to a cone. This ambiguity has to be resolved by measuring several photons from the source and by image reconstruction.
A second group of detectors is capable of measuring the direction of the recoil electron by tracking it. This enables the determination of the direction of motion of the scattered photon and allows to resolve the origin of the photon much more accurately: the Compton cone is reduced to a segment of the cone, whose length depends on the measurement accuracy of the recoil electron. "Modern type" Compton telescopes with a tracker, have the advantage that only fewer photons are needed to recover the position of sources, depending on background conditions and quality of the events. They are also inherently sensitive to polarization. However for all those advantages a price must be paid: the original photon is measured via several individual measurements at different interaction positions. Each of these introduces measurement

errors which are propagated into the recovery of the origin and energy of the photon. In addition, the complexity of the measurement process requires non-trivial techniques to find the direction of motion and origin of the photons.

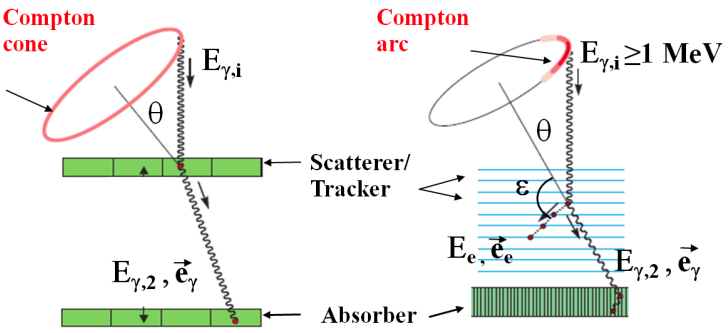

Figure 2.1: Comparison of two different Compton telescopes: a "COMPTEL type" instrument and a "modern type" instrument with a tracker (picture taken from https://www.med.physik.uni-muenchen.de/research/new-detectors/index.html).

2.2 The COMPTEL instrument

The *Compton Gamma-Ray Observatory (CGRO)*, launched in April 1991, performed the first full-sky survey in gamma rays. With four different instruments, CGRO, orbiting the Earth at nominal height of 450 km, operated over a wide range of photon energies from about 20 keV to 30 GeV:

- the *Energetic Gamma-Ray Telescope (EGRET)*: a spark chamber instrument for imaging of the energy range 20 MeV − 30 GeV;
- the *Imaging Compton Telescope (COMPTEL)*: an imaging gamma-ray telescope sensitive to photons between 1 and 30 MeV;
- the *Oriented Scintillation Spectrometer (OSSE)* for nuclear spectroscopy of selected regions in the energy range 0.1 − 10 MeV;
- the *Burst and Transient Source Experiment (BATSE)* with 8 scintillation detectors positioned to yield omnidirectional exposure.

COMPTEL, onboard CGRO, was the first successful Compton telescope put into space, opening the 1 − 30 MeV range as a new window to astrophysics. The schematic representation of the COMPTEL instrument is shown

in Figure 2.2. The detection principle of this telescope is a Compton scatter interaction in a plane of upper liquid scintillation detectors. The Compton scattered photon escapes this detector, and is absorbed in a second plane of NaI scintillation detectors at a distance of 150 cm. Measurement of interaction positions and energy deposits in both detector planes provide the information about the Compton scatter process.

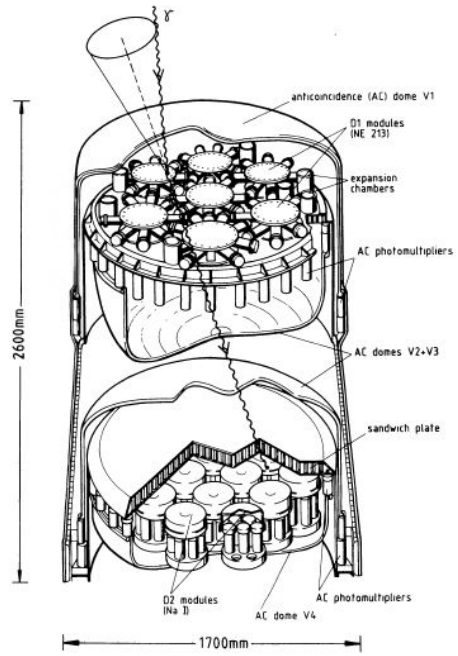

Figure 2.2: Schematic diagram of COMPTEL Instrument, as illustrated in [15].

In particular the upper detector plane, called D1, consists of seven modules, each of which is 28 cm in diameter and 8.5 cm deep. They are filled with liquid scintillator (NE213A), with properties of low Z and low density ($\rho \sim 1\text{g/cm}^3$). With a thickness of 8.5 cm, the D1 design optimizes the probability of a single Compton scattering process within a single D1 module. Each of the D1 modules is viewed by eight photo-multiplier tubes (PMTs). The D1 modules are mounted on a thin aluminum plate of 1.45 m in diameter, with holes cut out beneath the D1 modules. The high-voltage power supplies, the high-voltage junction boxes and the front-end electronics are mounted beneath the platform out of the gamma-ray path from D1 to D2. The lower detector plane, called D2, consists of fourteen modules (28.2 cm diameter and 7.5 cm thickness) made of scintillating inorganic NaI(Tl) crystals, with

properties of high Z to absorb the scattered photons. Each of the D2 modules is viewed by seven PMTs from below. The anode signals of the seven PMTs are summed and individually processed by the Front-End Electronics (FEEs). The D1 detector assembly has an active area of 4188 cm^2 and a total mass of 167.5 kg. while the D2 detector assembly has an active area of 8744 cm^2 and a total mass of 429.1 kg. Each of the D1 and D2 detector subsystems is completely surrounded by two active plastic charged-particle shields (veto domes) that are used in anti-coincidence with D1 and D2 detectors to reject charged-particle triggers. Each veto domes is made of thin plastic scintillator (1.5 cm thick) and viewed by 24 PMTs.

A COMPTEL event is defined by a coincident signal in the upper (D1) and lower (D2) detector within the proper time-of-flight window with no signal from any of the charged-particle shields. The measured parameters for each telescope event generated by gamma-ray photon are:

1. energy deposit of the Compton electron in upper detector;
2. location of the Compton scatter interaction in upper detector;
3. pulse shape of upper detector scintillation signal;
4. energy deposit of the scattered photon in lower detector;
5. location of the interaction in lower detector;
6. time of flight from upper to lower detector;
7. absolute event time.

From these raw parameters the useful quantities that describe the measured event can be easily derived. For example, the total energy deposit from the gamma ray is derived from the energy measurements in the upper and bottom detector planes:

$$E_{tot} = E_1 + E_2 \tag{2.1}$$

while the Compton scatter angle is derived from these energy measurements using the Compton formula (1.5).

The instrument operates in the range of 800 keV to 30 MeV with a field-of-view of ~ 1.5 steradians. The total energy resolution (FWHM) improves with energy from about 10% at 1 MeV to 5% at 20 MeV. The spatial resolution (1σ) at 1 MeV is approximately 2 cm for a D1 module and 1 cm for a D2

module. These energy and spatial resolutions translate through the Compton-scatter kinematics to an angular resolution of $1^\circ - 2^\circ$ again a function of total energy and zenith angle.
COMPTEL also measures the time sequence of the D1 and D2 interaction with the time-of-flight (ToF) system. The ToF measurement is defined as the time difference between the interactions in the D1 and D2 modules. The raw ToF values are used by the onboard electronics to distinguish down-scattered or forward-scattered events (D1 $\rightarrow$ D2) from up-scattered (D2 $\rightarrow$ D1) events.

2.3 COMPTEL performances

2.3.1 Effective Area

One of the basic measures of the instrument response is the telescope effective area (in units of cm^2) for point sources. The effective area is the product of the intrinsic efficiency with the projected geometric-area, and depends on the source direction and photon energy. Therefore, the effective area A_{eff} can be expressed as:

$$A_{eff}(\theta, \varphi, E) = A_{geo}(\theta, \varphi) \cdot \varepsilon(\theta, \varphi, E) \tag{2.2}$$

where ε is the intrinsic telescope efficiency depending on the specific data selections, the incident photon direction (θ, φ), and photon energy E. A_{geo} is the geometric area normal to the incident photon direction.

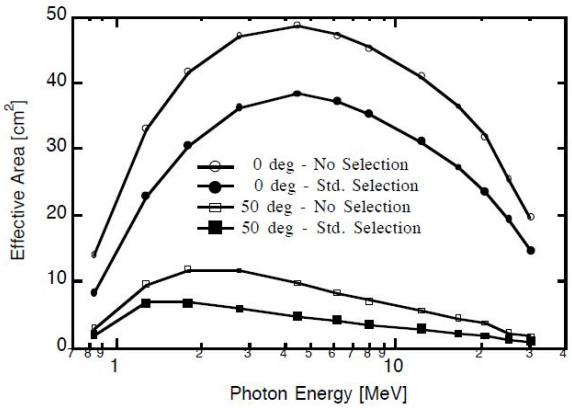

Figure 2.3: COMPTEL effective area as a funtion of the incident photon energy (picture taken from [18]).

The effective area of the instrument was in the range of 10 to 40 cm^2, dependent on energy. In Figure 2.3 the effective area computed using simula-

tions is shown as a function of energy, for two separate event-selection criteria and two incident angles. The low energy roll-over in A_{eff} is due to the D1 and D2 module energy thresholds, while at higher energies the decrease in the Compton-scatter cross-section becomes important.
To comparison with our analysis is important to point out that COMPTEL effective area at 1 MeV after quality cuts is around 10 cm^2.

2.3.2 Energy Responce

The measured energy spectra are characterized by a full-energy peak and a tail toward lower measured energy deposits, typically due to incomplete absorption of the scattered photons, as illustrated in Figure 2.4. In fact in many events either one or both the detectors may not contain the full interaction energy, i.e., secondary photons or particles escape the detector. As expected, the fraction of events with incomplete energy loss increases with energy. The fraction of events with total energy absorption decreases rapidly from 60% at $1-2$ MeV to $\sim 10\%$ at 10 MeV. The total energy resolution (FWHM) improves with energy from about 10% at 1 MeV to 5% at 20 MeV.

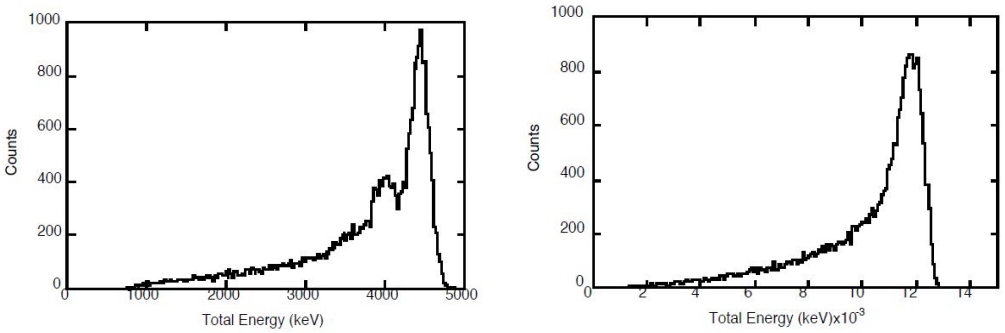

Figure 2.4: COMPTEL energy responce to a 4.430 MeV (left) and a 12.143 MeV (right) monoenergetic point source at normal incidence (pictures taken from [18]).

2.3.3 ARM Distribution

Another important quality in Compton Telescope is the *Angular Resolution Measure (ARM)*. In the ideal case with no measurement errors, ARM will be zero. In reality, energy and location measurement errors produce a finite width in the ARM measurement distributed about zero. In the case of COMPTEL this width is around $1^\circ - 2^\circ$, as a function of energy (see Figure 2.5, where

the ARM distribution for 4.430 and 12.143 MeV photons at normal incidence are shown).

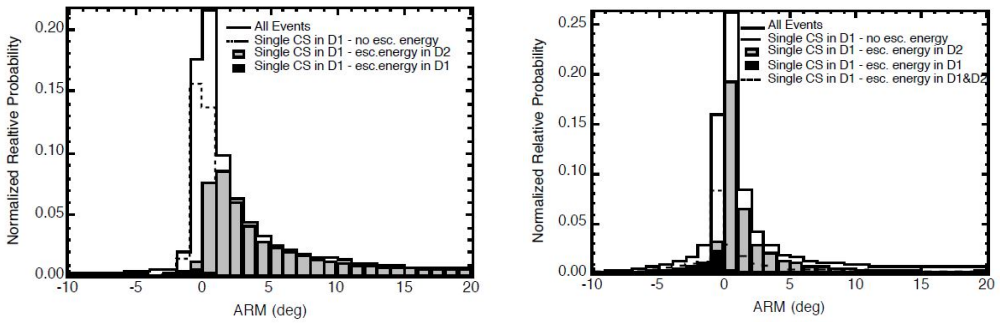

Figure 2.5: COMPTEL ARM distribution for a 4.430 MeV (left) and a 12.143 MeV (right) monoenergetic point source at normal incidence (pictures taken from [18]).

2.4 Lessons learnt from COMPTEL

Despite the results obtained by COMPTEL, gamma-ray sky in the MeV range remains largely unexplored, mainly because of the modest sensitivity achieved by this telescope. It becomes clearly evident considering Figure 2.6, where COMPTEL sensitivity is compared to the sensitivities so far achieved by other X and high energy gamma-ray observatories.

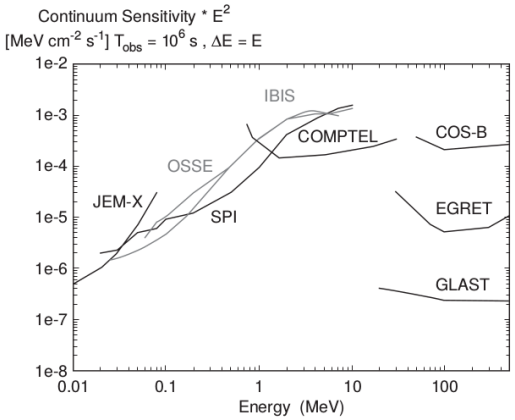

Figure 2.6: Illustration of the point source continuum sensitivity for different X and Gamma-ray Telescopes, as reported in [21].COMPTEL sensitivity is estimated for an observation time of 10^6 s.

Even INTEGRAL-IBIS is not able to fill the gap between hundreds of keV to 50 MeV, since its sensitivity is excellent only below-say 100 keV. Therefore the next generation low/medium-energy gamma-ray telescopes should have a sensitivity which is at least comparable to that achieved by EGRET at higher energies.
In the case of COMPTEL the sensitivity was mainly determined by the background event rate. In the original COMPTEL proposal to NASA the cosmic background was overestimated and the intensity level of locally produced background events was clearly underestimated. Furthermore it was found during the course of the mission that the background rate below 4.2 MeV steadily increased, due to the build-up of radio-active isotopes, such as ^{22}Na, ^{24}Na and others.

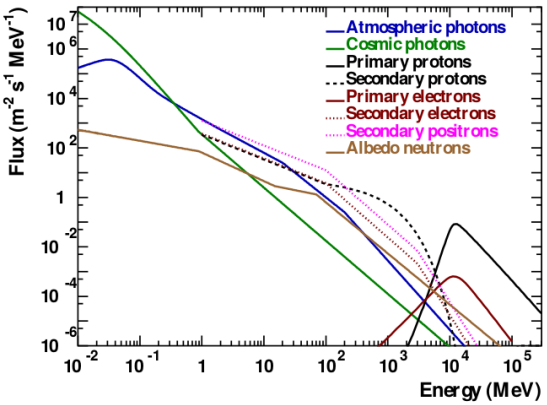

Figure 2.7: Background environment for an equatorial 550 km LEO orbit computed in the ASTROGAM proposal ([25]).

In order to gain the required increase in sensitivity for future telescopes, the background rate has to be minimized. There are different possibilities:

- to improve the detectability of point sources, having the best possible angular resolution is most effective;
- a very significant background reduction can be achieved by localizing the arrival direction on the event circle. This is possible, if the track of the Compton electron is measured. By this means the background per angular resolution element can be suppressed typically by a factor of 10;
- to minimize the production of secondary gamma-rays (the main background source of COMPTEL), it is essential to have as little passive ma-

terial around the instrument as possible, in order to reduce background production inside the anticoincidence and guarantee best performance, optimizing angular and energy resolutions;

- optimization of φ-selection windows and windows for scatter angle directions is another important and sensitive tool to reduce the background;
- the choice of the satellite orbit has a huge effect on the overall background. In particular, in *Low Earth Orbit* (LEO) albedo will be the biggest background source around 1 MeV (see Figure 2.7), while at higher orbits activation becomes a major issue.

2.5 General guidelines for a future Compton Telescope

Several Compton space missions have been recently proposed (like the ESA medium class mission ASTROGAM and the NASA medium class mission COMPAIR, only to name the two leading proposals nowadays), and will be presented again in an updated version in the coming years. However, all of these will rely on the silicon strip detector technology. Silicon trackers, largely applied to particle detection in the last two decades, provide good position and energy resolution and abide by many items listed before for background rejection.
Therefore, the payload for a future telescope optimized for the MeV regime (as proposed by the ASTROGAM Collaboration, in 2015) will consists of three main detectors:

- A **Silicon Tracker**, in which the cosmic gamma rays undergo a first Compton scattering or a pair conversion, based on the technology of *Double Sided Si Strip Detectors (Si DSSDs)* to measure the energy and the position of each interaction with an excellent energy and spatial resolution;
- A **Calorimeter** made of scintillating crystals readout by photodetectors, to completely absorb all secondary particles and measure the interaction position as well as the deposited energy. Thus it should be built of high-Z material (e.g. CsI) and have good position and energy resolution;
- An **Anticoincidence System** design with plastic scintillators covering the whole instrument to detect single charged relativistic particles with an efficiency exceeding 99.99% and to reject charged-particles background events.

The payload is completed by the front-end electronics, the back-end electronics, a payload data handling unit and a power supply unit. The Telescope will operate in LEO, at a nominal height of $550 - 600$ km, with a Field of View ≥ 2.5 sr. It will achieve an angular resolution $\leq 1.5°$ and a sensitivity (for an observation time of 1 month) $< 3 \cdot 10^{-5}$ MeV cm^{-2} s^{-1} at 1 MeV.
The COMPAIR collaboration is also examining the performances of a CZT-strip (Cadmium zinc telluride) calorimeter for the parts closest to the Tracker, where knowing the positions of the interacting low-energy Compton-scattered photons is very important. CZT calorimeters provide better spatial and energy resolutions than CsI(Tl) calorimeters, but have much higher costs.

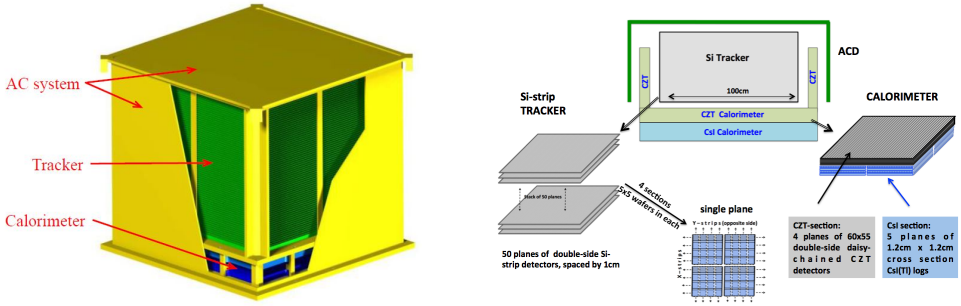

(a) ASTROGAM. (b) COMPAIR.

Figure 2.8: Schematic diagram for future Compton Telescopes, taken from [25] and [9].

Since the time scale for an M-class mission is around 10 years, with a cost $\sim$ 500 M€, there is the actual opportunity for a small CubeSat Telescope realization, with contained development costs, relatively quick design phase, to be used as a pathfinder test instrument for a future Compton Telescope.

Chapter 3

Silicon Tracker

3.1 Properties of a tracker for Compton Telescopes

As mentioned before, the tracker will be the heart of a future Telescope optimized in the MeV energy range, playing several tasks. First of all, it has to act as a Compton scattering and pair creation medium. Therefore the material requires a large cross-section for these interactions and low Doppler-broadening; for both reasons a low Z material is preferred. Secondly, it has to measure the direction of the secondary electrons and positrons as well as their energy very accurately.

Semiconductor detectors provides good position and energy resolution, and represent the most logical choice for the Tracker of a future Compton Telescope. In particular Silicon Detectors are preferred to Germanium Detectors for the following reasons:

- Silicon provides better angular resolution than Germanium assuming ideal detector properties, as shown in Figure 3.1. On average, the angular resolution worsens with increasing Z, but it also strongly depends on the shell structure of the individual atoms: the best FWHM is obtained for alkaline metals, while the worst FWHM is reached for noble gases, where orbitals are completely filled.

- Germanium detectors are very expensive and must be used at reduced temperature for proper operation (usually the liquid nitrogen temperature, 77.2 K). This fact is a great problem for space operations. Little Ge crystals detector is used in INTEGRAL-SPI however, for a space telescope, it is practically unrealizable to cover a great amount of volume

with Germanium detectors. Moreover the cooler system contribute to the increase of passive materials which activation could be a considerable source of background.

- the Silicon strip detector technology was already applied to the detection of gamma rays in space with the AGILE and Fermi-LAT missions. However, whereas AGILE and Fermi use Single Sided Strip Detectors (SSSDs), the tracker for a Compton Telescope needs Double Sided Strip Detectors, in order to obtain precise information on electrons direction.

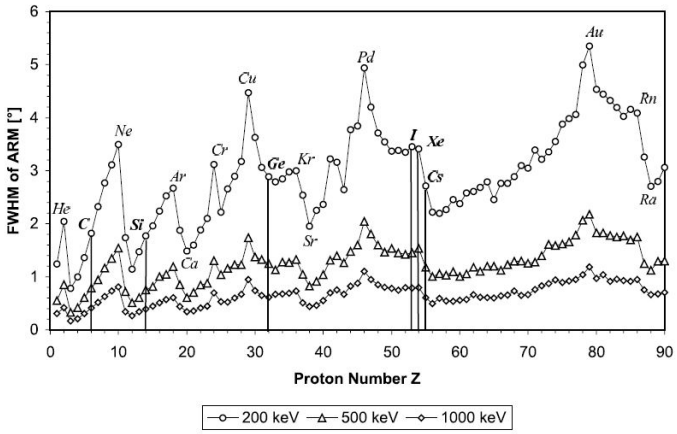

Figure 3.1: Angular resolution as a function of the atomic number Z, assuming ideal detector properties ([30]).

Therefore a Compton telescope based on semiconductor technology should use a Silicon tracker similar to the one used in Fermi-LAT, despite the energy resolution of Silicon is worse than that of Germanium.
However there are some differences from the tracker for a Compton telescope with respect to the one of Fermi-LAT. Firstly it should not have tungsten layers (which act as converter material in FERMI-LAT tracker) and have an ultra-light mechanical structure minimizing the amount of passive material within the detection volume. This enables the tracking of low-energy Compton electrons and reduce the effect of multiple Coulomb scattering and the background due to activation. Moreover a fine spatial resolution ($< 1/6$ of the microstrip pitch) is needed. These would be obtained by analog readout of the signals, as for the AGILE tracker. Finally an ultra low-noise front-end electronics is essential, in order to accurately measure the low energy deposits produced by Compton events with an excellent spectral resolution.

In the design of a tracker for a future Compton telescope many parameters must be carefully evaluated and tuned, like the number of the layers, the layers thickness, the strip pitch etc.
For example, a decrease of the strip pitch implies obviously a better spatial resolution. However it also implies the read-out of a much higher number of channel and then more power consumptions.
Moreover a much higher sensitive volume achieved with the increasing of the number of layers, involves a considerable increase in the pay-load costs.
The thickness of the silicon layers is an additional physical quantity that has to be carefully evaluated. In fact, when a charged particle pass through the volume of the silicon layer, undergoes several scattering due to the Coulomb interactions with lattice atoms. Usually to describe this phenomenon the *average scattering angle* is defined:

$$\theta = \frac{13.6\text{MeV}}{\beta cp} Z \sqrt{\frac{x}{X_0}} \tag{3.1}$$

where X_0 is the *radiation length*. Therefore, a much higher thickness for the layers, is reflected to large particles deviation and a greater error the trajectory reconstruction. Moreover the leakage current also increase. Instead, a much thick detector implies a smaller number of charge carriers and the decrease of signals intensity.

3.2 Noise in a Silicon strip detector

The key parameter for the design of a microstrip detector is the signal-to-noise ratio, S/N. In this section the various noise sources are described, and the dependence of the signal-to-noise ratio on the shaping time is discussed.

As illustrated in Figure 3.2, the detector is represented by the capacitance C_d and the detector bias voltage is applied through the bias resistor R_b. For the bias resistor holds the assumption $R_b \gg T_P/C_d$ where T_P is the peaking time of the shaper. In other words the bias resistor must be sufficiently large in order to block the flow of signal charge. In this way all of the signal is available for the amplifier. The bypass capacitor C_b, serves to shunt any external interference coming through the bias supply line to ground. The series resistor R_S represents any resistance present in the connection from the detector to the amplifier input, for example the resistance of the connecting wires, the resistance of the detector electrodes, etc. Finally the coupling

capacitor C_c at the input of the amplifier can be neglected in our analysis, since the capacitor passes AC signals.

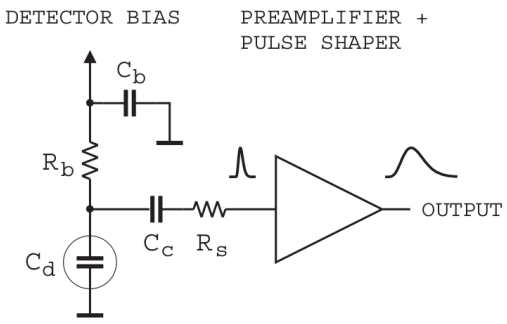

Figure 3.2: Detector front-end circuit (picture taken from [23]).

The electronic noise is usually expressed in term of the *Equivalent Noise Charge* (ENC), i.e. the input charge for which $S/N = 1$. The electronics noise sources, differentiated in noise voltage sources and current noise sources, are here summarized (a complete and thorough discussion of the argument can be found in [23]):

- *Detector bias current.* The noise current of the sensor is computed assuming that the input impedance of the amplifier is infinite, while the current that flow through R_b is negligible. The noise current will then flow through the detector capacitance, yielding a voltage:

$$v_{nd}^2 = 2q_e I_d \frac{1}{(\omega C_d)^2} \tag{3.2}$$

- *Parallel resistance.* The bias resistance R_b acts as a noise current source. In addition also the contribute of the sensor capacitance has to be taken into account:

$$v_{np}^2 = \frac{4kTR_b}{1 + (\omega R_b C_d)^2} \tag{3.3}$$

- *Series resistance.* The noise associated with the series resistance R_s is simply computed as:

$$v_{nr}^2 = 4kTR_s \tag{3.4}$$

- *Amplifier input noise voltage.* The noise sources associated with an amplifier are a white noise component and a $1/f$ noise component. Then the equivalent noise voltage is:

$$v_{na}^2 = v_{nw}^2 + \frac{A_f}{f} \tag{3.5}$$

In the case of a RC-CR shaper with equal differentiation and integration time constants ($\tau_i = \tau_d \equiv \tau$), the equivalent noise charge can be computed via the formula:

$$Q_n^2 = \left(\frac{\epsilon^2}{8}\right)\left[\left(2eI_d + \frac{4kT}{R_b} + i_{na}^2\right)\cdot\tau + (4kTR_S + e_{na}^2)\cdot\frac{C_d^2}{\tau} + 4A_fC_d^2\right] \quad (3.6)$$

In order to reach a good estimation of the equivalent noise ratio for the tracker designed in this thesis, the physical quantities in 3.6 was evaluated for a suitable microtrip detector (e.g. the silicon microstrip detector used in FERMI-LAT mission) and read-out electronics (e.g. the ASIC VATA460,[10]). The physical quantities settled for the equivalent noise ratio computation are listed in Table 3.1.

Parameter	Value
T	300 K
I_d	10 nA
R_b	40 MΩ
i_{na}	0.2 pA/$\sqrt{\text{Hz}}$
e_{na}	5 nA/$\sqrt{\text{Hz}}$
A_f	10^{-11} V^2
R_s	400 Ω
C_d	10 pF

Table 3.1: Parameters used for the equivalent noise charge estimation.

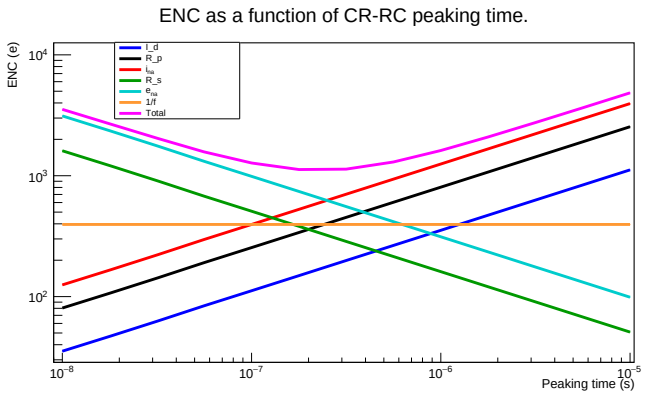

Figure 3.3: Equivalent noise charge as a function of the CR-RC peaking time.

The dependence of the ENC on the CR-RC peaking time is shown in Figure 3.3. As we can see voltage sources are the most important noise

source for short peaking times, while at long peaking times the current noise sources dominate. A minimum is reached when the current and voltage noise contributions are equal.
Since the shaping time of VATA460 is $\sim 2\mu$s, we can correctly assume an equivalence noise charge of $1100 - 1200\, e^-$ for our future tracker design.

Chapter 4

Detector design and simulations

4.1 The MEGAlib software package

Simulations are an essential analysis tool in physics, and play a fundamental role in the development and design of X and gamma-ray telescopes, in particular. In fact they allow determining the performance of the detectors with respect to the desired science objectives. In addition, they enable the optimization of the design by performing trade-off studies between variations of the detector setup, various instrument orbits, optimization of passive materials, and many more. Finally, simulations help to prepare and to understand calibrations and measurements of the instrument.
In this work simulations are made using the simulation and data analysis tool MEGAlib (the Medium Energy Gamma-ray Astronomy library), developed by Andreas Zoglauer. The MEGAlib software package is completely written in C++ and utilizes the ROOT software library for its graphical user interface and its data display. Its main application area is hard X-ray and low-to-medium-energy gamma-ray telescopes, from a few keV up to hundreds of MeV. MEGAlib encompasses the complete data analysis pipeline from simulations to high-level data analysis, thanks to its four principal libraries:

1. **Geomega (Geometry for MEGAlib)**. Geomega is the universal geometry and detector description library of MEGAlib, for the detailed modeling of different detector types: 2D or 3D strip detectors, drift chambers, calorimeters. The geometry file has to include the description of all materials, volumes and detectors properties of the telescopes (energy resolutions, noise properties, trigger criteria, etc.);

2. **Cosima (Cosmic Simulator for MEGAlib)**. Cosima is the simula-

tion tool of MEGAlib. It is based on Geant4 and provides the generation of simulated data, via electromagnetic (Livermore and Penelope) or hadronic libraries. In this work the Livermore library is used for the simulation of monochromatic point-like photon sources at different energies, and diffuse sources;

3. **Revan (Real Event Analyzer)**. Revan provides the events reconstruction using the detector characteristics and the energy and position informations of individual hits. Its task is to identify the original interaction process such as photo effect, Compton scattering, pair creation, radioactive decay etc. This is a crucial step in the data-analysis framework since the overall performance of a Compton telescope is not only determined by its hardware but also by the performance of the algorithms which recover the original parameters of the incident photons from the measured (or simulated) data. In fact each not recognized or incorrectly reconstructed event lowers the efficiency and increases the background of the instrument, affecting the final sensitivity estimation of the telescope. Revan events reconstruction tries to identify the most simple structures like pair events and muons first; searching for the much more complex structures of Compton events in the remaining events. The events reconstruction process consists of four main steps:

   - Clusterize into one hit the single passing particle interactions in two or more adjacent voxels of a strip or pixel detector;
   - Search for high energy events like a vertex of the pair events or a muon tracks;
   - Search for Compton electron tracks and the Compton interaction sequences;
   - Search for special beta-decays.

4. **Mimrec (MEGAlib image reconstruction)** Mimrec is MEGAlib's main tool for advanced data analysis. It enables event selections on various parameters of Compton and pair events, and provides analysis of energy spectra, ARM distributions, Compton and pair image reconstruction etc.

Moreover, during the thesis work, several scripts and macros were written in C++ and Python, in order to reach much more control on various parameters and kinematic variables.

4.2 Defining detector's geometry: Starting geometry

As mentioned before, the purpose of the thesis is to design and evaluate the performances of a CubeSat Compton Telescope. A CubeSat is a standardized model of miniaturized satellite for space research, with precise restrictions both in volume and in weight: it consist in a $10 \times 10 \times 10$ cm^3 cube with a maximum weight of 1.33 kg (1U cubesat). It is possible to increase the cubesat length of one axis, adding one unit of the same dimensions. Thus a 2U cubesat ($10\times10\times20$ cm^3) or a 3U cubesat ($10\times10\times30$ cm^3) can be realized.

The telescope fundamental design, shown in Figure 4.1, is composed of two main detectors: a silicon strip tracker unit, with the dimensions of $8.4 \times 8.4 \times 7.5$ cm^3 on the upper half, and a CsI(Tl) calorimeter, with the dimensions of $8.9 \times 8.9 \times 5$ cm^3 on the lower half, leaving some space for structural elements, electronics and other passive materials (not considered at this stage). The first design was settled "back of the envelope", making several educated guesses which evaluated both performance and costs.

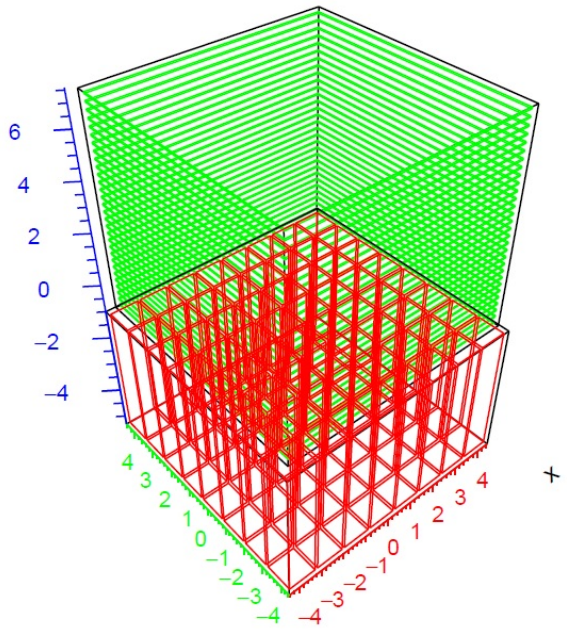

Figure 4.1: Schematic diagram of the telescope starting geometry.

The tracker, which fundamental parameters are listed in Table 4.1, is

made of 30 double-sided silicon strip detectors layers stacked along the z-axis. Each layer has a thickness of 500 μm and a pitch of 150 μm both in x and y direction, which should allow good electron-tracking capabilities. As regards the signal readout, several ASIC can be taken into account; for example, VATA460 has an acceptable input range of 95 fC, adequate shaping time ($\sim$ 2 μs), power consumption (0.3 mW/chn) and trigger capabilities. A 10 bit digitization gives a reading accuracy of 2.1 keV while the electronic noise is around 4.3 keV, that is an equivalent noise charge of 1200 e^-, as we can estimate from Figure 3.3.
Given these parameters, the energy resolution can be computed: in the energy range studied, it is around $\sim$ 5 keV.

The calorimeter is made of an array of 8×8 CsI(Tl) bars. Each bar has dimensions of $1.0 \times 1.0 \times 5$ cm^3 and a depth resolution of 1.5 cm [1]. CsI(Tl) scintillators are quite cheap and provides adequate density (4.5 g/cm^3) and yield ($\sim$ 50 ph/keV). Moreover the wavelength of maximum emission of 550 nm is very convenient, matching a readout based on Silicon photodiodes (Hamamatsu S3590, for example) or Silicon photomultipliers (SiPMs). The fundamental parameters are listed in Table 4.1, and more informations about calorimeter description and optimization can be found in [1].

Parameter	Value or range
Tracker size	$8.4 \times 8.4 \times 7.5$ cm^3
Number of layers	30
Layers thickness	500 μm
Strip pitch	150 μm
Guard ring	1 mm
Readout electronics	VATA460
Energy resolution (1 σ)	$\sim$ 5 keV from 100 keV up to few MeV
Electronical noise	1200 e^-
Bit digitization	10

Table 4.1: Tracker main parameters for the starting geometry.

The trigger used for the first simulation was very simple, requiring at least one hit in the tracker and one in the calorimeter. Moreover an anti-coincidence system, designed with plastic scintillators, can be easily added to this basic design. Covering the whole instrument, the anti-coincidence system would

[1] The depth resolution is chosen similar to the one for the Fermi LAT

detect single charged particles with an efficiency of 99.99%, and veto nearly all the charged particle background. At this stage no ACD was considered in this design.

Parameter	Value or range
Calorimeter size	$8.9 \times 8.9 \times 5$ cm^3
CsI(Tl) bars dimension	$1.0 \times 1.0 \times 5$ cm^3
Photodiode readout	Hamamatsu S3590
Readout electronics	VATA460
Depth resolution	1.5 cm
Energy resolution (1 σ)	from 10 keV at 100 keV to 25 keV at 2 MeV

Table 4.2: Calorimeter main parameters for the starting geometry.

4.3 First simulations

The geometry defined in the previous section was tested using *Cosima*, simulating the detectors response under a monochromatic point-like photon source at normal incidence and at different energies: 100, 333, 500, 1000, 2000 keV. In this way the behavior and the performance of the telescope as a function of the energy, can be analyzed. For each set of simulations we are interested, in particular, in the energy and ARM (*Angular Resolution Measure*) spectra of the reconstructed photon. In fact, from these spectra, some of the fundamental parameters for the characterization of the detector as the energy and angular resolution, and the effective area can be obtained.

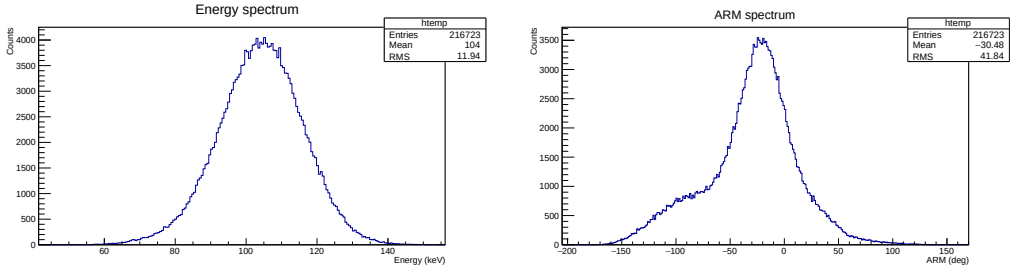

(a) Energy spectrum. (b) ARM spectrum.

Figure 4.2: Energy and ARM spectra for the 100 keV simulation with the starting geometry.

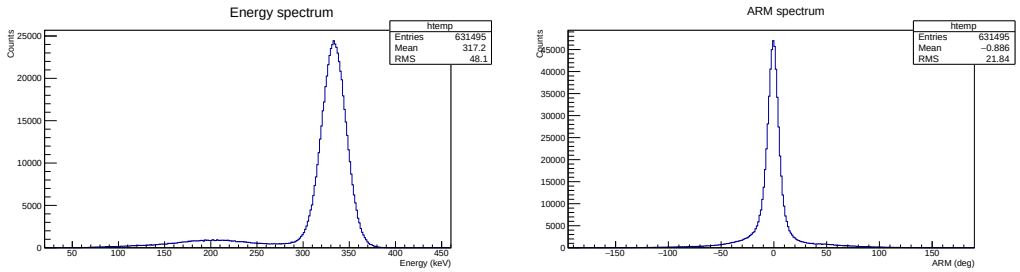

(a) Energy spectrum. (b) ARM spectrum.

Figure 4.3: Energy and ARM spectra for the 333 keV simulation with the starting geometry.

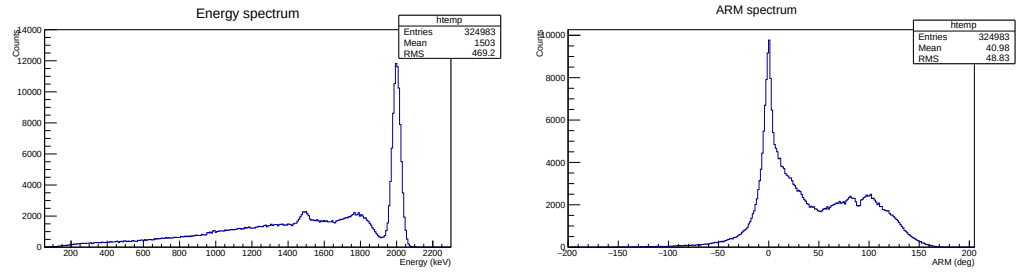

(a) Energy spectrum. (b) ARM spectrum.

Figure 4.4: Energy and ARM spectra for the 2 MeV simulation with the starting geometry.

In Figure 4.2, Figure 4.3 and Figure 4.4 some examples of the energy and ARM spectra resulting from the simulations can be seen.
The energy spectra of reconstructed photons are characterized by a full-energy peak and a tail toward lower energy deposits due to incomplete particles absorption. Therefore, to estimate the energy resolution we can simply fit the full absorption peak with a Gauss distribution and compute the ratio between the FWHM and the centroid of the curve.
Moreover for the simulation at 2 MeV we can notice a little peak around ~ 1.5 MeV. This is due to the fact that for energies above few MeV, there is an increasing contaminations of pair events wrongly reconstructed as Compton events. In fact, when the positron produced in a pair event annihilates, one of both produced gamma-ray can escape from the detector. Thus the reconstruction algorithm could not found a vertex for these pairs, and the events are misclassified as Compton events. The results is a peak at the energy of $E - 511\,\text{keV}$ (single photon escape). Instead, the peak at the energy

of $E - 1022\,\mathrm{keV}$ (double photon escape) is not observed in our simulations, since the escape of both photon is a quite unlikely circumstance, especially in the energy range studied. Obviously these wrongly reconstructed events contribute also to the tails in the ARM distribution.

The ARM spectra are a bit more complex, since they can exhibit left or right tails, due to incompletely absorbed scattered gamma ray and recoil electron, respectively. These phenomena are remarkable especially at lower energies ($\sim$ 100 keV) and at higher energies ($\sim$ 2000 keV). As a consequence, the shape of the peak is affected by the tails of poorly reconstructed events and can not be correctly fitted by any simple distribution, neither a Gauss or a Lorentz distribution. A quite good estimation of the peak FWHM can be obtained with a fit of two different gauss distributions to take into account the different tails for each side of the peak.

Finally, the effective area A_{eff} can be computed using the formula:

$$A_{eff} = A_{start} \frac{N_{measured}}{N_{simulated}} \tag{4.1}$$

where $N_{measured}$ is the number of reconstructed events in the simulations, and $N_{simulated}$ is the total number of simulated events. Instead, A_{start} is the area from which the simulated particles are started. In order to simulate plane waves from distant astrophysical sources with *Cosima*, the start area is defined by the concept of the surrounding sphere. The particles are started from a disk on the surface of the surrounding sphere, with the same radius R of the sphere itself (see Figure 4.5); thus A_{start} is simply computed as πR^2.

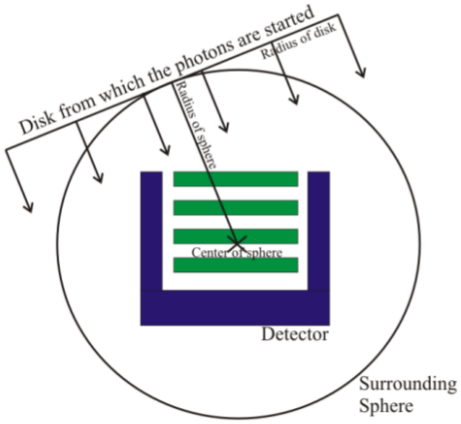

Figure 4.5: Illustration of the concept of the surrounding sphere (picture taken from *Cosima* manual).

In Table 4.3 the telescope main parameters are shown as a function of simulated energy.
In this phase of the work the errors are only statistical and not particularly significant (they can be reduced at discretion increasing the number of simulated events). Under these conditions systematic errors are more relevant, but in this preliminary stage of the work they were not studied (the final structure of the detector is not decided yet, no passive materials were included in the design etc.). In the completely settled design where the detectors characteristics, the read-outs and the electronics performances are all decided and evaluated, it will be possible to carefully compute the systematic errors.

Energy [keV]	A_{eff} [cm^2]	Energy resolution (FWHM)	ARM FWHM [°]
100	1.43	24%	51.5
333	3.90	9.3%	12.9
500	3.62	6.8%	9.9
1000	2.81	4.2%	8.6
2000	2.49	2.7%	11.5

Table 4.3: Telescope performances for the starting geometry.

The obtained performances are very sensitive to energy. The effective area increases rapidly from 100 keV to 333 keV and then starts to slowly decrease, due to the lowering of Compton cross section at higher energies. At the same time, the energy resolutions and the ARM FWHM greatly improve from 100 keV to 333 keV. Even considering these preliminary results, we can see that the 100 keV energy establish the lower limit for the CubeSat design. Instead, the higher limit is set to energies of few MeV, since already at 2 MeV the rate of wrongly reconstructed events starts to increase (as it can be seen from the tails in the energy and ARM spectra in Figure 4.4).

4.4 Only-calorimeter geometry

Before moving on with the analysis and the optimization of the detector, it is interesting to understand, in a very simple but straightforward way, how much the presence of the silicon tracker affect the overall performance of the telescope.

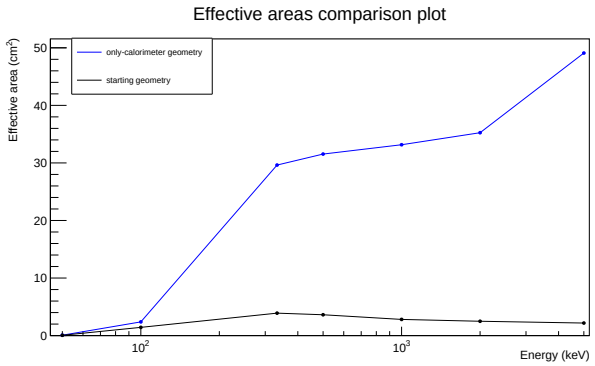

Figure 4.6: Comparison of the effective areas estimated from *only-calorimeter configuration* and *starting configuration*.

To achieve this scope an *only-calorimeter geometry*, made only of an 18×18 array of $0.5 \times 0.5 \times 10$ cm^3 CsI(Tl) crystals was tested. Obviously this is a quite unrealistic design; nevertheless such a simple geometry can give important informations about the necessity of the presence of the tracker.
As we can easily expect, the effective area of the *only-calorimeter geometry* is much bigger than the one computed for the *starting geometry* (Figure 4.6). However the increase of the effective area is followed by a remarkable worsening of the ARM spectra for different energies. As we can see in Figure 4.7 and Figure 4.8, many wrongly reconstructed events contribute not only to the increase of the tails of the distributions, but also to the broadening of the peak. In fact, in order to give just a rough estimation, if in the *starting geometry* the ARM FWHM is around $\sim 10°$ for energies above 100 keV, in the *only-calorimeter geometry* the FWHM is around $25° - 30°$.

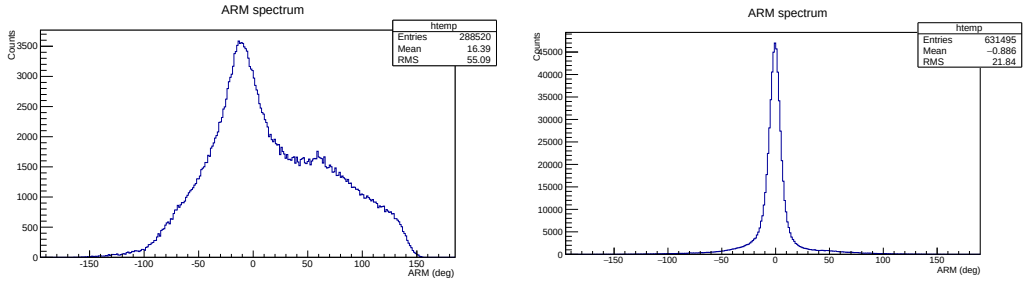

Figure 4.7: Comparison of the ARM spectrum from only calorimeter configuration (left) and starting configuration (right), for a 333 keV simulation.

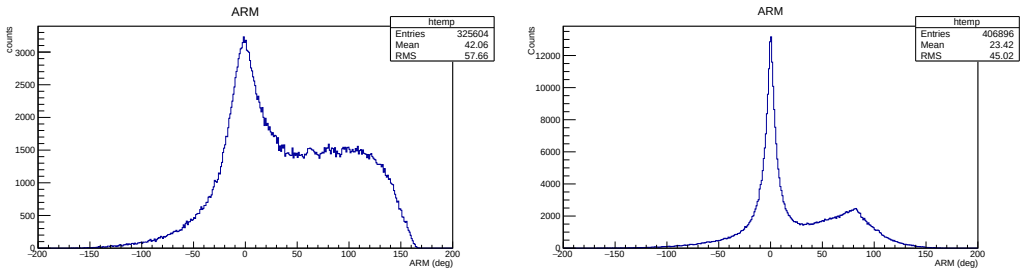

Figure 4.8: Comparison of the ARM spectrum from only calorimeter configuration (left) and starting configuration (right), for a 1 MeV simulation.

Finally, there are not great differences in the energy spectra of the two configurations (in Figure 4.9 an example for the simulation at 1 MeV is presented). Therefore from these simulations we have a straightforward indication of the importance of a silicon tracker.

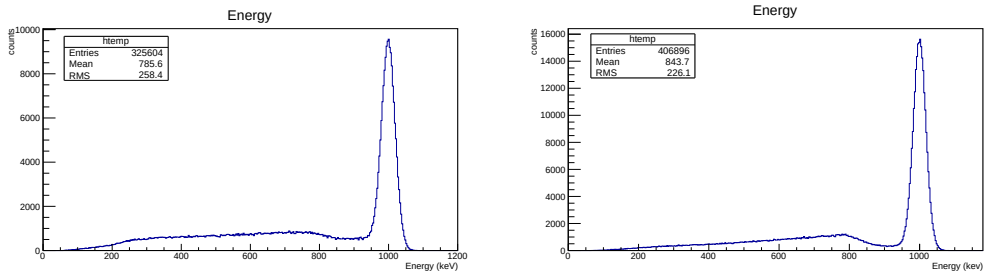

Figure 4.9: Comparison of the energy spectrum from only calorimeter configuration (left) and starting configuration (right), for a 1 MeV simulation.

4.5 Lateral calorimeter geometry

In the *starting geometry* a significant fraction of events are lost at the edge of the tracker, as it can be seen in Figure 4.10, where the events projection on the x-y plane for a 333 keV simulation is shown. This is due to the fact that for energies below 1 MeV the majority of photons are scattered to angles $> |30°|$ (see the Klein-Nishina cross section in Figure 1.5). Thus, there is a high probability that the scattered particles escape the detector without leaving any hits.

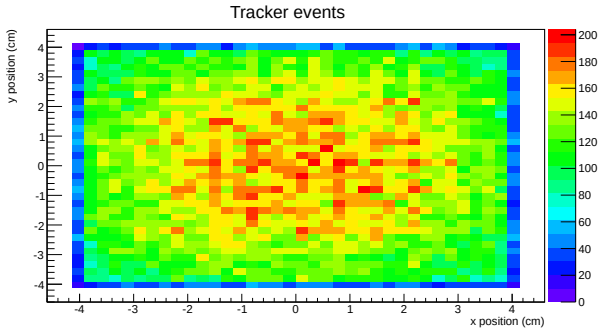

Figure 4.10: Events distribution in the x-y plane for a 333 keV simulation.

Therefore we decided to study in more detail a new geometry, including a lateral calorimeter made of $1.0 \times 1.0 \times 8.1$ cm^3 CsI crystal, decreasing the x-y size of the tracker and the bottom calorimeter (see Figure 4.11)[2].
In particular we tested two configurations: in the first one (we will name it *lateral calorimeter 1 geometry*) the *starting detector* size was decreased of 0.8 cm both in x and y direction; in the second one (named *lateral calorimeter 2 geometry*) the x and y size was reduced of 1.8 cm.

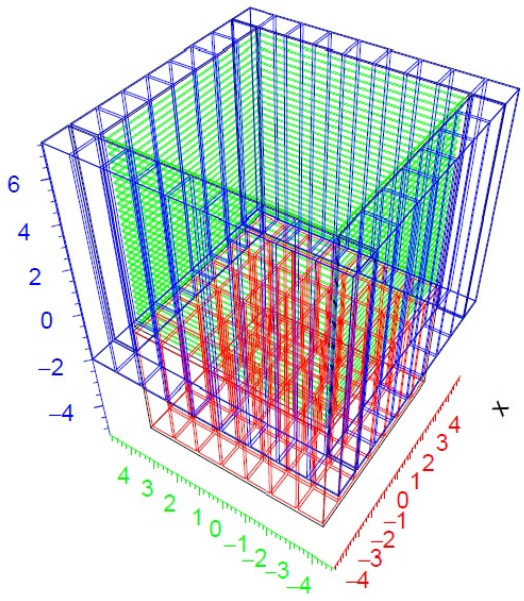

Figure 4.11: Schematic diagram of the telescope final geometry.

[2]we decreased the tracker and bottom calorimeter sizes in order to still have a configuration compatible to a 2 *mathrmU* CubeSat

As shown in Figure 4.12, the effective area estimated for both configurations increases compared to the one estimated for the *starting geometry*. However the effective area of the *lateral calorimeter 1 configuration* is greater than the one estimated for the *lateral calorimeter 2 configuration*. The energy and ARM FWHM, instead, are comparable for each configuration.
The considerable increase in the effective area achieved with the introduction of lateral CsI(Tl) crystals, brings the choice of the detector geometry to a satisfying stage. In fact, from our analysis the best configuration is *lateral calorimeter 1 geometry*, since a design with a more effective area is, of course, preferable under comparable values for the others final parameters of space telescope, as the energy and angular resolution.

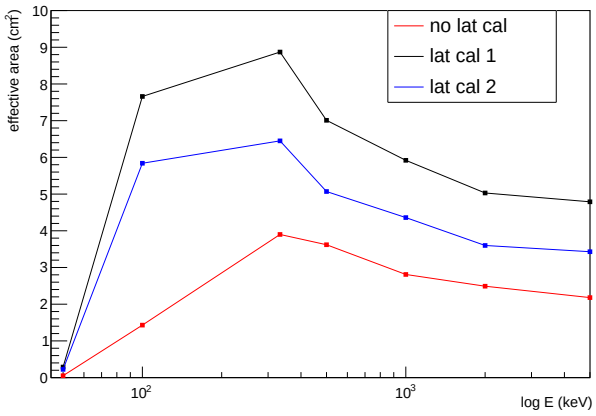

Figure 4.12: Effective area estimated from simulations with and without lateral calorimeters.

Energy [keV]	A_{eff} [cm^2]	Energy resolution (FWHM)	ARM FWHM [°]
100	7.09	25%	55.4
333	8.67	9.3%	14.6
500	6.87	6.9%	11.1
1000	5.81	4.4%	10.9
2000	4.95	2.8%	13.7

Table 4.4: Telescope performances for the *lateral calorimeter geometry*.

In Table 4.4 the telescope main parameters for this final geometry are shown as a function of simulated energy. In comparison to COMPTEL, in the energy range around 1 MeV, the detector developed in this thesis can provide

better energy resolution but worse ARM values, due to the impossibility of time-of-flight measurements.

4.6 Performances under pair production

In this section the telescope performances regarding the pair detection are briefly analyzed. In fact, in this work pair production analysis plays a role of secondary importance compared to Compton scattering, mainly because of two different reasons:

- in the energy range studied (from 2 MeV up to 10 MeV) pair production cross section is quite small so we can not reach a substantial effective area with any feasible detector design;

- pair production enables a significantly more straightforward determination of the origin of the photon, so pair events analysis would be much more simple compared to the Compton scattering one.

For pair production, simulations for the energy of 2, 3, 4, 5, 8 and 10 MeV were made, considering again point-like photon sources at normal incidence. In Figure 4.13 and Figure 4.14 some examples of the spectra obtained are shown. The incomplete particles absorption visible in the energy spectra becomes a quite relevant problem at energies above $\sim$ 5 MeV, while the peak in the *Point Spread Function* or PSF distribution (which describes the response of an imaging telescope to point objects), becomes narrower with the increase of the energy.

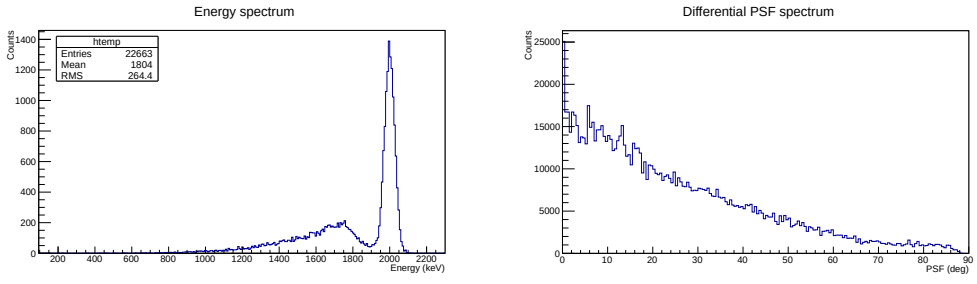

(a) Energy. (b) Differential PSF.

Figure 4.13: Energy and PSF spectra under pair detection for the 2 MeV simulation.

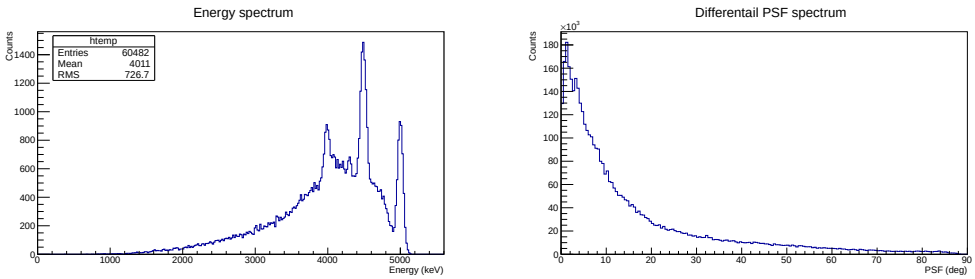

(a) Energy. (b) Differential PSF.

Figure 4.14: Energy and PSF spectra under pair detection for the 5 MeV simulation.

The effective area obtained from the pair simulations is compared to the one associated to Compton scattering events in Figure 4.15: the effective area for pair events is actually quite small. Moreover, for the energies above 5 MeV, a significant fraction of incompletely absorbed events affects the values obtained, and the peaks due to the escape of one or both photons in positron annihilation events are very pronounced.

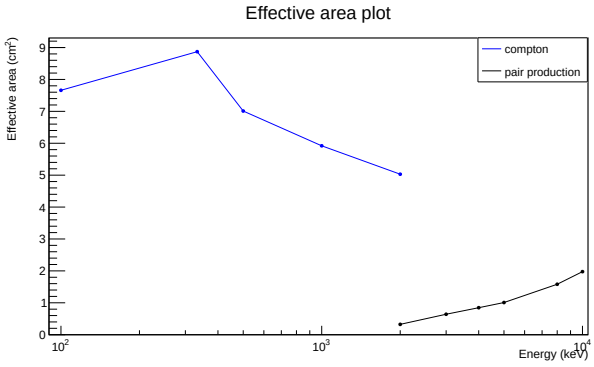

Figure 4.15: Comparison of the effective area for Compton scattering and pair production.

On the other hand the PSF can be easily improved applying quite simple cuts: cuts in the direction of positrons and electrons were performed, excluding events with a small angle with the tracker plane. The PSF containment intervals greatly improved (from the red to the green line, and from the black to the blue line in Figure 4.16) discarding no more than $20 - 25\%$ of the total events. Another task of quality cuts is to remove misclassified Compton events, which is important especially at lower energies.

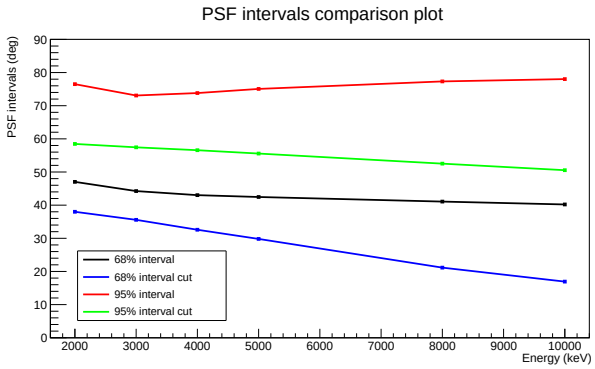

Figure 4.16: PSF containment intervals before and after quality cuts.

Chapter 5

Event selection and tracker optimization in the Compton regime

5.1 Tracked events and event selection

In **Chapter 4** the telescope geometry was defined and the general performances were estimated with satisfying results. In this chapter we want to perform further analyses. We only considered Compton scattered events, ignoring performance of reconstructions of pairs (as explained before pair production plays a role of secondary importance compared to Compton scattering in our detector design). We selected and divided the total events in event classes. In particular tracked events present a very different topology respect to not tracked events.

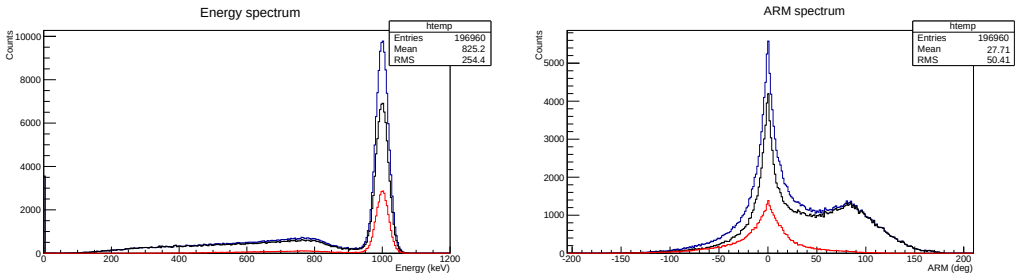

(a) Energy. (b) Differential ARM.

Figure 5.1: Energy and ARM spectra for tracked and not tracked events in a 1 MeV simulation.

In Figure 5.1 tracked and not tracked events are plotted for the 1 MeV simulation: in blue are represented total events, in black not tracked events and in red tracked events. As we can see, tracked events represent only a small fraction of the total data. Moreover the ARM distribution does not exhibit the left and right tails due to incompletely absorbed events, but it present a broadened peak.
In addition to the energy resolution and the ARM FWHM, another parameter can be computed for tracked events: the *Scatter Plane Deviation* or SPD.
In Figure 5.2 an example of SPD distribution for a 1 MeV simulation is plotted. As is can be seen, for tracked events the SPD HWHM is around roughly $30 - 40°$, depending on energy. Otherwise, for not tracked events, the SPD HWHM is set to 180°. Therefore tracked events can still provide much better informations compared to not tracked events, despite the broadening of ARM peak.

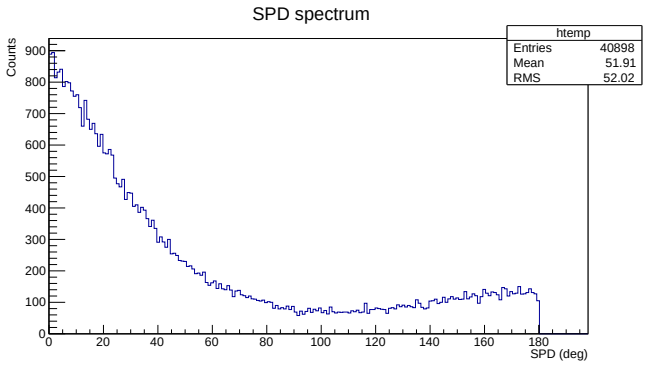

Figure 5.2: SPD distribution for a 1 MeV simulation.

Thus, to further improve our analysis, we decided to divide the events reconstructed in simulations in four different event classes:

- **class 1 events**: events with a track and at least one hit in the bottom calorimeter, but no hits in the lateral calorimeter. The parameters estimated for this events class are plotted in **blue** in the following figures of this chapter;

- **class 2 events**: events with a track and at least one hit in the lateral calorimeter, but no hits in the bottom calorimeter. The parameters estimated for this events class are plotted in **black** in the following figures;

- **class 3 events**: events with a single hit in the silicon tracker (thus not tracked) and at least one hit in the bottom calorimeter, but no hits in the lateral one. The parameters estimated for this events class are plotted in **red** in the following figures;
- **class 4 events**: events with a single hit in the silicon tracker (not tracked) and at least one hit in the lateral calorimeter, but no hits in the bottom one. The parameters estimated for this events class are plotted in **green** in the following figures.

We omitted in our analysis tracked and not tracked events with hits both in the bottom and in the lateral calorimeter, since they hardly represent properly reconstructed events in our configuration, that constitute only a small fraction of total events. We also omitted events with hits in the lateral and in the bottom calorimeter but with no hits in the tracker, since the performances are worse and in this work we are interested in optimizing the silicon tracker performance.

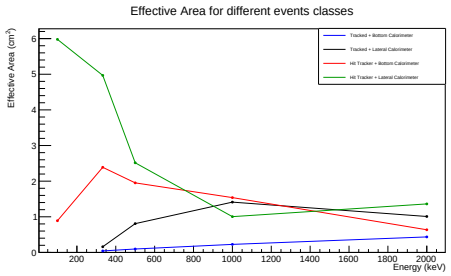

(a) Effective area.

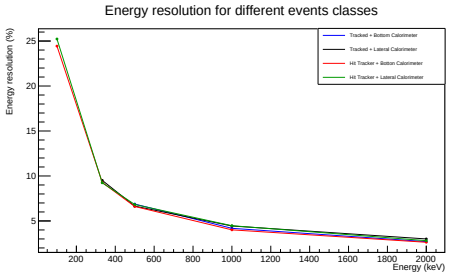

(b) Energy resolution.

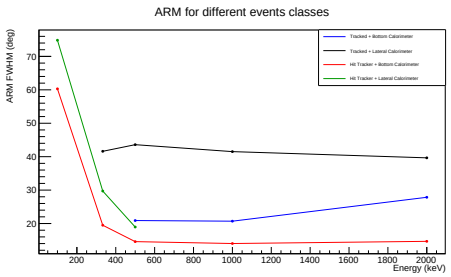

(c) ARM FWHM.

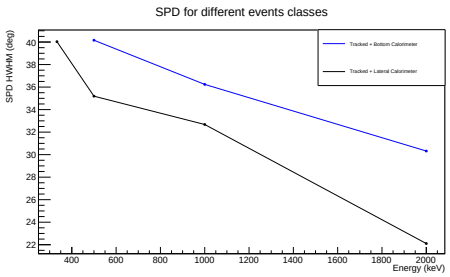

(d) SPD HWHM.

Figure 5.3: Parameters estimated for the standard configuration.

In Figure 5.3 the main telescope parameters are plotted as a function of energy for each different class considered. The fit of the ARM and energy

spectra were made as explained in **Chapter 4**, while the fit of the SPD distribution was performed via an half-gaussian. As we can see, the energy resolutions are nearly the same for all event classes, while tracked events present an ARM FWHM highly worse than not tracked events. In fact in order to generate an electron track, a sufficient amount of energy needs to be transferred to the electron. This results in large Compton scatter angles, where energy measurements uncertainties have a larger influence on the angular resolution than at small Compton scatter angles.

Moreover some points are not present in the figures. In fact in the case of the 100 keV energy, we do not have any tracked events, since an electron with energy smaller than a hundred of keV is completely absorbed in a 500 μm thick silicon layer. Instead, at higher energies the 1 cm thick lateral calorimeter can not completely absorb the scattered particles, so a fit of the ARM spectra could be very difficult due to the large presence of the tails in the distribution.

Parameter	Simulated values
Layers number	20, 25, **30**
Layers thickness	400, **500**, 600 μm
Layers pitch	50, **150**, 300 μm
Bit digitization	8, **10**, 12
Equivalent noise charge	600, **1200**, 2400 e^-

Table 5.1: Parameters considered for the silicon tracker optimization. In bold are reported the parameters used in the standard configuration.

In order to optimize the tracker design, and validate the characteristics and the specifics settled in **Chapter 4**, related both to the detector design and the read-out electronics, many simulations were performed. Starting from the *standard configuration* defined in the previous chapter, we stressed time by time a single physical quantity (as the number of tracker layers, the pitch of the strip, the noise level etc.) and computed the main parameters useful to define the telescope performance. In Table 5.1 are listed the physical quantities considered in the simulations and the values investigated.

5.2 Layers number simulations

In the *standard configuration* the number of tracker layers was set to 30. Now we want to evaluate the performance of a silicon tracker with 20 layers and one with 25 layers. In order to not make this chapter too long-winded, for these and following tested configurations the results obtained are shown in **Appendix B** (in Figure B.1 and Figure B.2, in this case).
Moreover, to contrast the values obtained for these configurations to the ones obtained for the *standard configuration*, only the most important comparison plots are shown, in this and in the following sections.

A quick look to Figure B.1, Figure B.2 and Figure 5.3 is just enough to point out that there are no significant differences in the ARM and SPD values, and in the energy resolution for the different simulations, while we observe a great increase of the effective area with the increase of the number of layers. This is quite obvious, however it is still important to quantitatively evaluate this increase since the silicon tracker will constitute the most expensive element in the payload of such a prototype instrument. In Figure 5.4 the effective areas for tracked events in the different simulations are compared: in the left plot tracked events with a hit in the lateral calorimeter are shown, while in the right plot are shown tracked events with hits in the bottom calorimeter. As we can see a great increase of the effective area is obtained, for both event classes with a number of 30 layers in the tracker. For reference, the effective area for events with lateral calorimeter hits increases as $2 : 2.5 : 3$, so directly proportional to the layers number, as expected. This tell us that efficiency is directly proportional to the money invested in the tracker. Apparently the same consideration does not hold for tracked events with bottom calorimeter hits for lower energies.

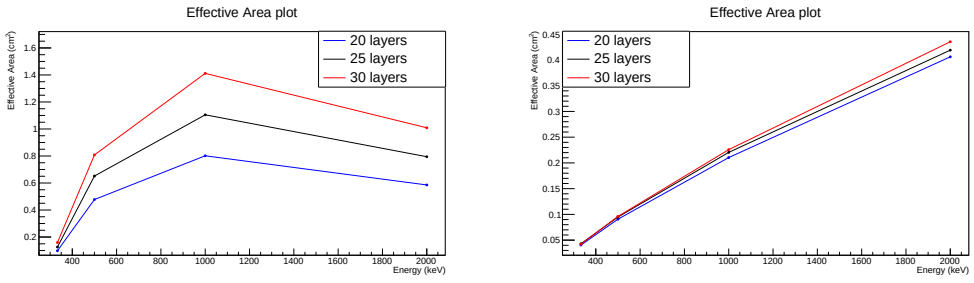

(a) Tracked plus lateral calorimeter events. (b) Tracked plus bottom calorimeter events.

Figure 5.4: Comparison of the energy resolutions for the simulations with different number of layers.

5.3 Layers thickness simulations

The second parameter considered in this analysis is the thickness of the layers. We stressed the initial value of 500 μm, and performed simulations for a 400 μm and a 600 μm layers thick tracker. The number of layers was also modified, since we want now to evaluate the telescope performance considering an equal amount of sensitive volume for the detector. Thus, the 400 μm thickness simulations was performed considering a tracker with 38 layers, while the 600 μm was performed considering a tracker with 25 layers.

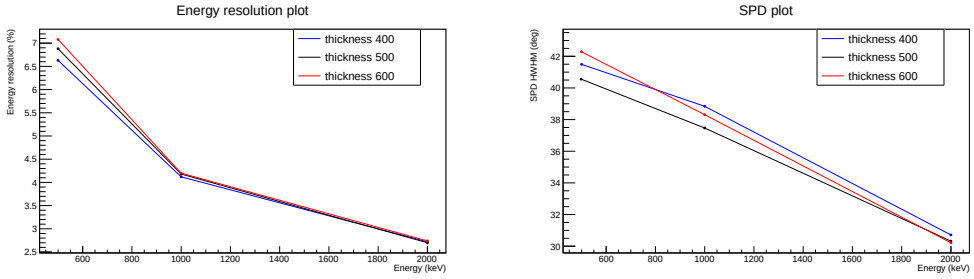

(a) Energy resolution. (b) SPD HWHM.

Figure 5.5: Parameters comparison for the simulations with different thickness for the layers (tracked + bottom calorimeter events).

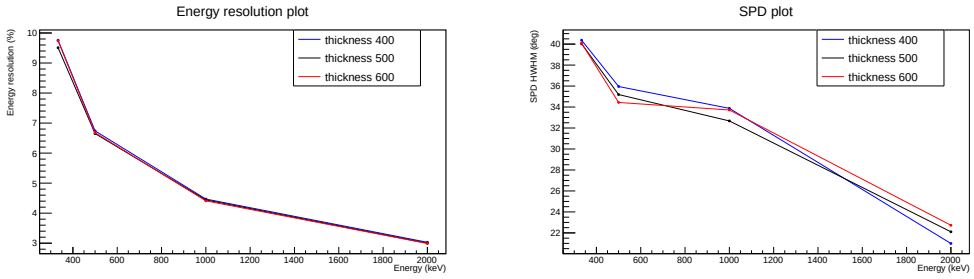

(a) Energy resolution. (b) SPD HWHM.

Figure 5.6: Parameters comparison for the simulations with different thickness for the layers (tracked + lateral calorimeter events).

The results obtained for the different events classes considered are shown in Figure B.3 and Figure B.4. No significant differences was found in any parameter estimated: in Figure 5.5 and Figure 5.6 some examples can be found for tracked events with hits in the bottom either in the lateral calorimeter.

As we can see the energy resolution is nearly the same for all of three configurations tested, and the differences in the SPD HWHM values are less than 5%. The same considerations hold for the ARM distribution. Therefore in the range studied, the choice of layers thickness does not affect very much the overall performance of the telescope.

5.4 Strip pitch simulations

While in the *standard configuration* the pitch of the strip was set to 150 μm, the performance of the detector with a strip pitch of 50 μm and 300 μm was evaluated too.
For these simulations the minimum length for clusterization in the data reconstruction algorithm was adjusted, in order to have at least a distance of 3 strip for an acceptable cluster in every configuration. Undoubtedly a decrease of the strip pitch implies a better spatial resolution. On the other hand it also implies the read-out of a much higher number of channels and then more power consumptions, so silicon strip pitch is a physical quantity that has to be carefully evaluated in the design of the tracker.

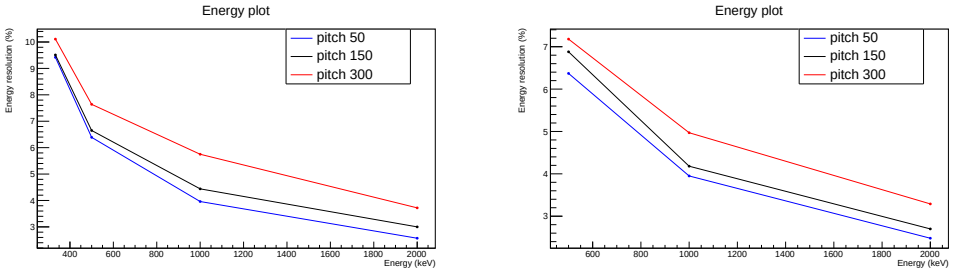

(a) Tracked plus lateral calorimeter events. (b) Tracked plus bottom calorimeter events.

Figure 5.7: Comparison of the energy resolutions for the simulations with different strip pitch.

In Figure 5.7 the energy resolution obtained for the 50 μm, 150 μm and 300 μm simulations for tracked events are compared. The energy resolution fairly improve from the configuration with 300 μm strip pitch to the configuration with 150 μm strip pitch, while the improvement is much less evident from 150 μm to 50 μm. Therefore we could keep 150 μm as a compromise of cost vs performance.
One the other hand the values estimated for the ARM FWHM and the SPD HWHM are practically the same for all configurations. An example is shown

in Figure 5.8 where the ARM FWHM for all three configurations are plotted, for tracked events with hits in the lateral calorimeter (the values at the top of the figure with rectangular markers) and for tracked events with hits in the bottom calorimeter (the values at the bottom of the figure with circular markers). This analysis validate the fairness of the choice of a 150 μm pitch for the silicon strip.

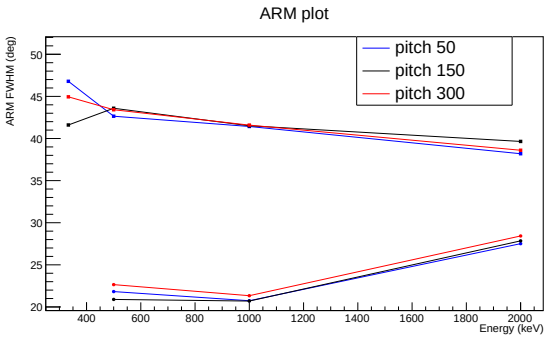

Figure 5.8: Comparison of the ARM FWHM for simulations with different strip pitch.

5.5 Bit digitization simulations

Simulations with 8 and 12 bit digitization for the analog readout of the signals were performed, and the results are shown in Figure B.7 and Figure B.8 (the *standard configuration* foresaw a 10 bit digitization).
We can observe an improvement in the energy resolution but no significant differences in the ARM and SPD values.

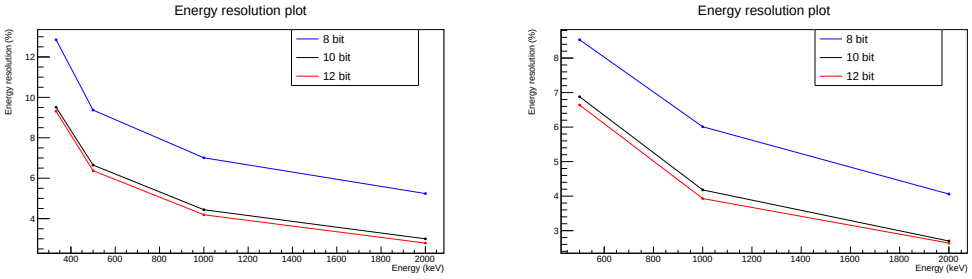

(a) Tracked plus lateral calorimeter events. (b) Tracked plus bottom calorimeter events.

Figure 5.9: Comparison of the energy resolutions for the bit digitization simulations.

As shown in Figure 5.9, the improvement is much more pronounced from the 8 bit to the 10 bit simulation than from the 10 bit to the 12 bit simulation. Thus, a 10 bit digitization for the signals readout is a more than adequate value in our design.

5.6 Equivalent Noise Charge simulations

In the *standard configuration* an equivalent noise charge of $\sim 1200\ e^-$ was estimated considering a 2 μs shaping-time for the readout electronics of a reasonable designed silicon microstrip detector (see Figure 3.3).
Now we want to evaluate the performance of the detector assuming a 600 e^- and a 2400 e^- equivalent noise charge. The results obtained with for simulations at different energies are shown in Figure B.9 and Figure B.10.
Quite obviously no considerable differences in the ARM and SPD values were observed, while the energy resolution greatly worsen with the increasing of the electronic noise. However it is very important to point out that the worsening is significant from the 1200 e^- ENC simulation to the 2400 e^- ENC simulation, while little differences subsist between the 600 e^- ENC and the 1200 e^- ENC simulations. Moreover, as we can see in Figure 3.3 an equivalent noise charge of 600 e^- would not be reasonably achieved for our detector (without a significant redesign of the electronics), so this value has to be considered as a lower limit in our prototype. Therefore the results obtained with these simulations can be considered as a good validation of the fairness in the choice of the ASIC proposed for signals read-out.

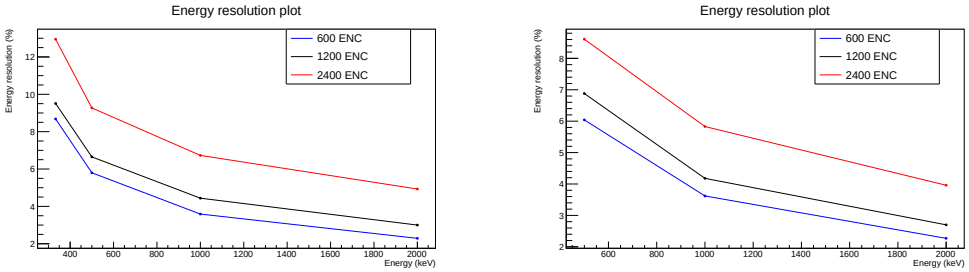

(a) Tracked plus lateral calorimeter events. (b) Tracked plus bottom calorimeter events.

Figure 5.10: Comparison of the energy resolutions for the different noise simulations.

Chapter 6

Background and sensitivity estimation

6.1 Background events

The next step in our analysis is to include background sources in the simulations, in order to achieve more realistic conditions for the detector. In a real-life space telescope there are four main sources of background, here briefly summarized:

- *Extragalactic gamma-ray background*: the EGB is a diffuse and isotropic photon background, mainly due to unresolved sources plus a possible diffuse component.

- *Earth albedo*: Earth albedo is due to the interaction of the cosmic rays with the upper atmosphere producing gamma-rays. In Low Earth Orbit, the orbit in which such a prototype will operate, earth albedo is the major source of background in our telescope;

- *Charged particles background*: there are many sources of charged particles, both extragalactic and galactic which may contribute to background. A continuos flux of charged particles composed by protons, electrons, positrons and light nuclei would run over the detector. However the majority of this radiation can be effectively shielded using an anticoincidence detector. Thus we estimate that the contribution of this background would be comparable to the EGB background in a real-life telescope.

- *Material activation*: the telescopes materials become radioactive due to the continuous incidence of charged and uncharged particles. Finally a

equilibrium between radioactive nuclei production and their decays is reached. This source of background is very difficult to treat since the activation of passive materials produce events inside the anticoincidence shield. Fortunately in LEO, the background due to passive materials activation is negligible compared to the ones due to earth albedo and the EGB, especially for such a small payload as the one we are considering here.

In this phase of the work we simulated Earth albedo and EGB background events, only in the half of the sky in which the detector was pointing. Therefore the albedo we are considering is the fraction of events wrongly reconstructed as coming from the top of the detector. Considering the high flux of albedo events, this is still the dominant component in our analysis. The charged background events are assumed to be roughly two times the events computed for the EGB. In Figure 6.1 the Albedo and EGB spectra are shown for a 6 hours simulation, in the region from 800 keV up to 20 MeV. For both spectra the events number rapidly decreases with the increasing of the energy. Moreover the ratio between albedo events and EGB events is ~ 15.

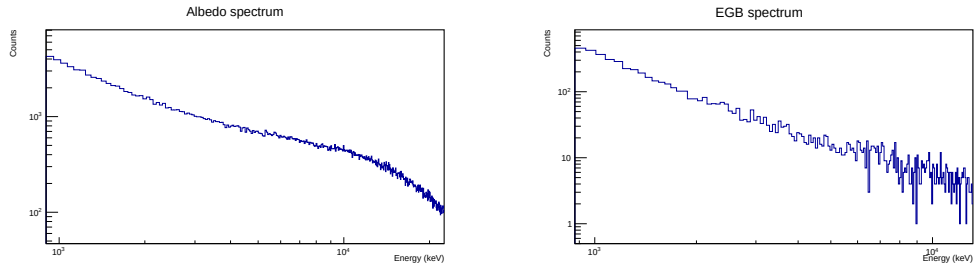

(a) Albedo. (b) EGB.

Figure 6.1: Albedo and EGB simulated counts spectra (log scale).

In this chapter we plan to thoroughly evaluate the performance of the selected detector structure, therefore in place of several monochromatic point sources we simulated signal events in the half of the sky in which the detector was pointing. The source was simulated using a power-law of the form:

$$\frac{dN}{dE} = N_0 \left(\frac{E}{E_0} \right)^{\gamma} \tag{6.1}$$

where N is the number of photons simulated, E is the energy, and γ is the energy index. In our simulation the energy index γ is set to -1 and the flux is

isotropic in angle. The source generates than a constant number of particles per zenith solid angle and per energy decades.
The estimated parameters depend now both on the energy and the zenith angle. An example can be found in Figure 6.2 where the effective area is computed in energy and zenit angle bins for tracked events with hits in the lateral calorimeter.

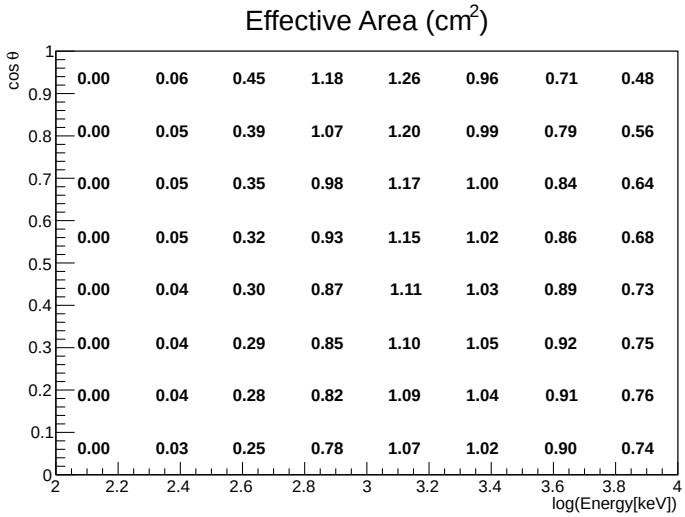

Figure 6.2: Effictive area for different energies and zenit angles for tracked plus lateral calorimeter events.

6.2 Sensitivity estimation

The final and most important parameter computed to describe any gamma-ray telescope performance is its sensitivity. The sensitivity describes the weakest source which can still be detected with a certain significance z (in units of σ). Actually, three types of sensitivities can be determined for a gamma-ray telescope:

- **continuum sensitivity**: the continuum sensitivity represents the minimum flux (in photon or in energy) of a continuous source needed to distinguish it from the background, with a certain significance level z;

- **line sensitivity**: the concept to estimate the line sensitivity is the same of the continuum one. The only difference is that in this case the source is distinguished from the background via the flux measurements of a single and specific nuclear lines;

- the **polarization sensitivity** which is the key parameter to judge the telescope performance under polarization measurements.

The continuum sensitivity is the only one computed in this work. However also the line and the polarization sensitivities will be interesting parameters for the determination of the performance of a completely designed instrument.

The continuum sensitivity F_z was calculated as explained in [30], through the equation:

$$F_z = \frac{z\sqrt{N_S N_B}}{T_{eff} A_{eff}} \tag{6.2}$$

where N_S is the number of source photons, N_B is the number of background photons, A_{eff} is the effective area of the telescope and T_{eff} is the effective observation time. Finally z, as explained before, is the significance level for which the source can still be detected. In this work, like in the majority of cases, the significance level is set to $z = 3$.
The number of source photons can be computed as:

$$N_S = F_z T_{eff} A_{eff} \tag{6.3}$$

Thus, substituting this value in (6.2) and solving for F_z the expression simplifies in:

$$F_z = \frac{z^2 + z\sqrt{z^2 + 4N_B}}{2T_{eff} A_{eff}} \tag{6.4}$$

Finally the number of background events N_B has to be computed in the resolution element. We can write:

$$N_B = F_B A_{eff} T_{eff} \Delta\Omega \tag{6.5}$$

with F_B flux of the background events and $\Delta\Omega$ resolution element, described by the ARM and SPD as follow:

$$\Delta\Omega = 2\pi\Big[\cos(\bar{\varphi} - \sigma_{ARM}) - \cos(\bar{\varphi} + \sigma_{ARM})\Big] \cdot \frac{2\sigma_{SPD}}{2\pi} \tag{6.6}$$

where $\bar{\varphi}$ is the average Compton scatter angle, σ_{ARM} is the ARM FWHM and σ_{SPD} is the SPD HWHM.

Energy bin [MeV]	A_{eff} [cm^2]	σ_{ARM} [°]	σ_{SPD} [°]	$\bar{\varphi}$ [°]	F_B [ph $cm^{-2}s^{-1}sr^{-1}$]	$\Delta\Omega$ [sr^{-1}]
$1 - 1.78$	0.29	17.0	32.5	72.0	$35.0 \cdot 10^{-3}$	0.63
$1.78 - 3.16$	0.39	24.1	28.9	50.2	$16.4 \cdot 10^{-3}$	0.63
$3.16 - 5.62$	0.32	19.0	25.2	23.4	$9.3 \cdot 10^{-3}$	0.23

Table 6.1: Parameters used for the sensitivity calculation for *tracked plus bottom calorimeter events*.

Energy bin [MeV]	A_{eff} [cm^2]	σ_{ARM} [°]	σ_{SPD} [°]	$\bar{\varphi}$ [°]	F_B [ph $cm^{-2}s^{-1}sr^{-1}$]	$\Delta\Omega$ [sr^{-1}]
$1 - 1.78$	1.26	32.7	26.9	86.4	$35.0 \cdot 10^{-3}$	1.01
$1.78 - 3.16$	0.96	40.0	20.2	56.9	$16.4 \cdot 10^{-3}$	0.76

Table 6.2: Parameters used for the sensitivity calculation for *tracked plus lateral calorimeter events*.

Energy bin [MeV]	A_{eff} [cm^2]	σ_{ARM} [°]	σ_{SPD} [°]	$\bar{\varphi}$ [°]	F_B [ph $cm^{-2}s^{-1}sr^{-1}$]	$\Delta\Omega$ [sr^{-1}]
$1 - 1.78$	0.96	15.1	180	28.1	$35.0 \cdot 10^{-3}$	1.54
$1.78 - 3.16$	0.72	19.1	180	22.6	$16.4 \cdot 10^{-3}$	1.58

Table 6.3: Parameters used for the sensitivity calculation for *not tracked plus bottom calorimeter events*.

We computed the sensitivity for the different event classes studied in the previous chapter and for different energies range. The estimated parameters used in the sensitivity calculation are listed in Table 6.1, Table 6.2 and Table 6.3. The sensitivity for not tracker events with hits in the lateral calorimeter was not computed since, as explained on the previous chapter, we do not have good estimations of the ARM values for these simulations. The observation time was set to 10^6 s and a significance level of $z = 3$ was assumed.

	Energy range		
	$1 - 1.78\,[\text{MeV}]$	$1.78 - 3.16\,[\text{MeV}]$	$3.16 - 5.62\,[\text{MeV}]$
Tracked + Bot Cal	$8.4 \cdot 10^{-4}$	$5.0 \cdot 10^{-4}$	$2.6 \cdot 10^{-4}$
Tracked + Lat Cal	$5.1 \cdot 10^{-4}$	$3.5 \cdot 10^{-4}$	
Not tracked + Bot Cal	$7.2 \cdot 10^{-4}$	$5.7 \cdot 10^{-4}$	

Table 6.4: Sensitivity expressed in $\text{ph}\,\text{cm}^{-2}\,\text{s}^{-1}$ for different events classes.

In Table 6.4 the sensitivity is computed for different events classes and different energy intervals. At present the sensitivity estimated for the designed detector is worse than that achieved by COMPTEL (the COMPTEL sensitivity around 1 MeV was about $\sim 2 \cdot 10^{-4}\text{ph}\,\text{cm}^{-2}\,\text{s}^{-1}$, as we can see from Figure 2.6). However it has to be pointed out that the one computed in this thesis is only a preliminary estimation of the detector sensitivity. No significant quality cuts was performed yet so there is the actual opportunity to greatly improve this estimation and to obtain a sensitivity better than the one achieved by COMPTEL.

Chapter 7

Conclusions

In this thesis the performance of a CubeSat Compton telescope was evaluated. This telescope should be used as a pathfinder test instrument for recently proposed medium-class Compton missions. In fact the ESA mission ASTROGAM and the NASA mission COMPAIR will be presented in an updated version in the coming years. Since the time scale for the development of an M-class mission is around 10 years, with substantial costs, the realization of a pathfinder instrument with contained development costs and a relatively quick design phase, is of great interest.
Such a CubeSat telescope should have a payload's dimension of 2U (i.e. $10 \times 10 \times 20$ cm^3) and would be composed of an upper silicon tracker and two CsI(Tl) calorimeters: a bottom calorimeter and a lateral calorimeter that surrounds the tracker. The telescope will operate in the energy range from 100 keV up to few MeV. In fact, as we evaluated in the thesis the energy of ~ 100 keV represents the lower limit for our detector, since the energy and angular resolution greatly worsens at this energy. Moreover the absence of tracked events and the increasing of the cross section for Photoelectric effect at energies below-say 100 keV make this region difficult to study. On the other hand the instrument would hardly operate at energies above few MeV, since the rate of wrongly reconstructed events for energies around 5 MeV is remarkable. This limit is barely improvable, since we would need much more material to fully absorb higher photons. However, this option can not be realized in the design of such a compact space telescope, since a CubeSat has precise restrictions both in volume and weight.
In **Chapter 4** the detectors design was settled and the first performances of the telescope were evaluated. Compared to COMPTEL, the best instrument to date the range around 1 MeV, such a instrument has a better energy resolution, but worse ARM values, due to partially absorbed events and the impossibility of time-of-flight measurements which impacts on the gamma

background rates. In **Chapter 5** further analyses are presented, selecting and dividing the total events in different classes (e.g. tracked and not tracked events). Many simulations were performed, in order to optimize the detector design and validate the characteristics settled both for the tracker geometry and the read-out electronics (e.g. number of tracker layers, silicon strip pitch, noise etc.). Simultaneously a similar work was performed for the calorimeter optimization (see [1]) and a final design of the telescope was settled.
Finally, in **Chapter 6** the first estimation of the telescope continuum sensitivity is computed, for different events classes and different energy intervals. At present the sensitivity estimated for the designed detector is worse than that achieved by COMPTEL. This is mostly due to the great presence of albedo background events. To avoid this problem two different solutions can be possible. First of all we can consider an higher orbit for our detector. In our design the telescope will orbit in *Low Earth Orbit* (LEO), at a nominal height of $450 - 500$ km. An higher orbit (e.g. *High Earth Orbit*, HEO) implies a smaller rate of albedo background events, but the background due to passive material activation becomes remarkable. This is a great complication, since material activation produces events inside the anticoincidence shield. Moreover an higher orbit also implies an increase of the launch costs and more difficulties in data communications, making this solution hardly realizable, especially for a small CubeSat mission.
The other possibility is to implement new algorithms and perform significant quality cuts in order to drastically differentiate background and wrongly reconstructed events, from properly reconstructed events. In this way, in the next future there is the actual opportunity to greatly improve the estimation presented in this thesis and to obtain a sensitivity better than the one achieved by COMPTEL.

Appendix A

Quality cuts

From our analysis the best configuration designed is the *lateral calorimeter 1 configuration* defined in **Chapter 4**. A further step is to find good criteria to differentiate poorly reconstructed events from properly reconstructed events. As we have seen, this is especially important at lower energies ($\sim$ 100keV) and at higher energies ($\geq$ 1000 keV) where the ARM spectra exhibit considerable left and right tails, due to incompletely absorbed particles. To achieve this scope some quality cuts were performed. These cuts were performed without considering background events, since they were meant only to understand the topology of wrongly reconstructed events. Thus, the obtained results are still preliminary; therefore they are included in an appendix and not in the main body of the thesis. However they are very important in order to reach a general understanding of how the telescope works, and will be useful to develop more complex and effective cuts in the future.
We first looked for possible anomalies in the events reconstruction considering the *Compton quality factor* given back in the output of our simulations. The *Compton quality factor* is computed from the Spearman Rank correlation coefficient to find the most probable combination of the paths the particles might have taken in the interaction with the telescope detectors (more details can be found in [30]). Although a Compton quality factor cut would be the most logical choice, it does not improve very much the ARM spectrum. It can be seen in Figure A.1 where we kept the 80% events with best quality factor values. Therefore we looked for other possible cuts involving other kinematics variables as cuts in the scattering angles and in sequence length (i.e. the number of hits in the reconstruction sequence).

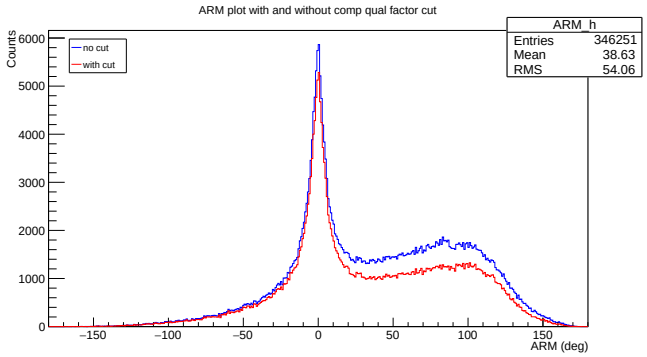

Figure A.1: ARM spectrum for a 2 MeV simulation with and without cuts.

In many cases more complex combinations of kinematic variables are needed, and there is not possible to check every possibility manually. To further improve the quality of our cuts the TMVA (*Tool for MultiVariate Analysis*) library from ROOT was used. In particular we used the *boosted decision tree* method. A training data sample is divided by the user in a signal sample and in a background sample; then, the *boosted decision tree* method identifies automatically the data as either signal or background, via the consecutive comparison respect to the set of various variable useful in the data analysis. The data are structured in a tree with the initial source split into subsets based on an attribute value test. The process is repeated several times; finally the data are classified as either signal or background, and the variables are ordered in statistical importance, depending on how many times they were used to separate signal from background. In this way the procedure performed with the training data sample can then be applied to the entire set of data. The accuracy of the method depends on the number of variables involved and the number of the tree node settled by the user.

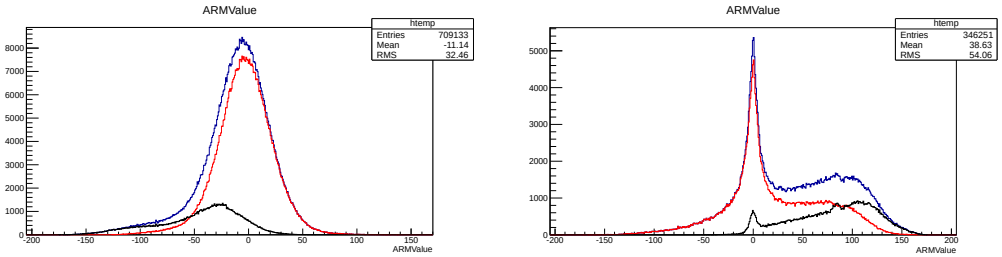

(a) ARM spectrum 100 keV. (b) ARM spectrum 2000 keV.

Figure A.2: Example of some spectra with and without quality cuts.

Firstly we performed TMVA cuts on single energy spectra and secondly we applied the TMVA procedure to a total spectrum with a final training sample composed of multiple energies data (in order to obtain final cuts independent on the energy of the sample). The signal was defined as all the events with $-20 \leq ARM \leq 20$ (central peak), while the remaining events are classified as background. Moreover the number of nodes was set to 4, that is a quite simple and unrealistic number for definitive quality cuts, but in this phase we want to manually reconstruct the trees in order to understand the variables importance in the procedure. With every single cut a fraction of $20 - 25\%$ of the total events was discarded and some examples are presented in Figure A.2: the histogram in blue represents the total data, in black the rejected data are plotted, and in red are represented the data after quality cuts. As we can see at the energy of 100 keV a great fraction of biased events is rejected, while at the energy of 2 MeV we can observe the decreasing of the events in the right tail.
As shown in Figure A.3 with the cuts performed some parameters, such as the ARM containment intervals and the ARM bias greatly improve.

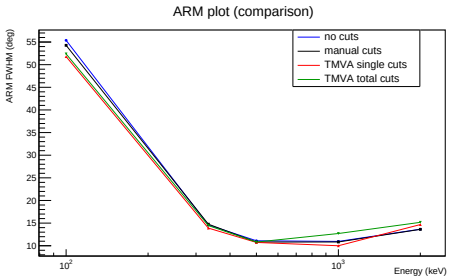

(a) ARM FWHM.

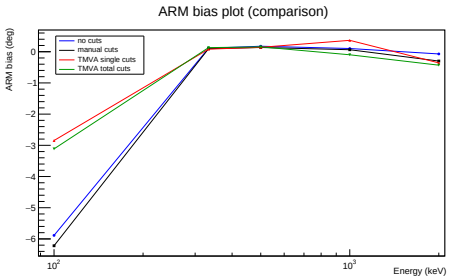

(b) ARM bias.

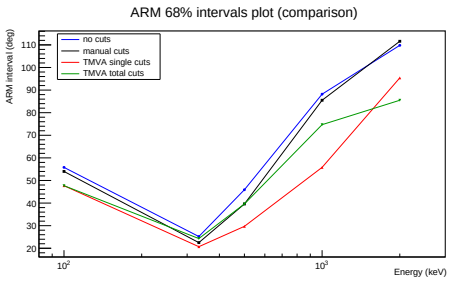

(c) ARM 68% interval.

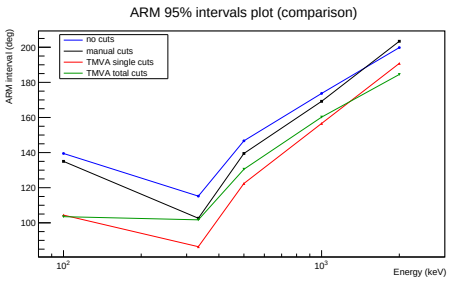

(d) ARM 95% interval.

Figure A.3: Results after quality cuts.

Appendix B

Tracker optimization plots

Layers number simulations

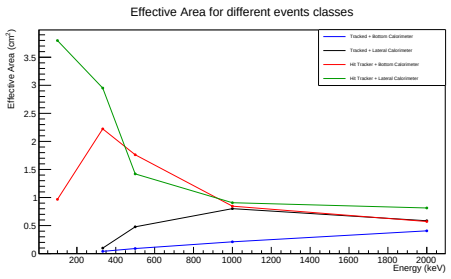

(a) Effective area.

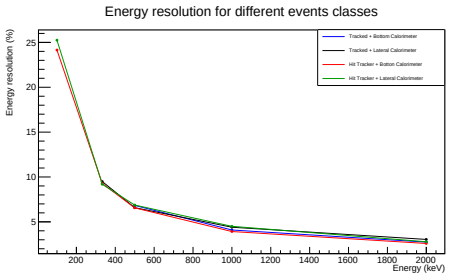

(b) Energy resolution.

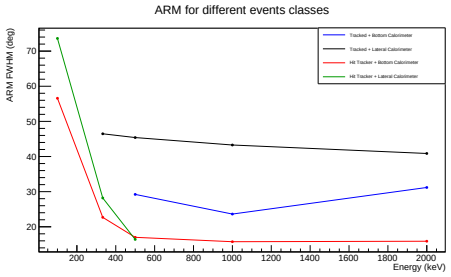

(c) ARM FWHM.

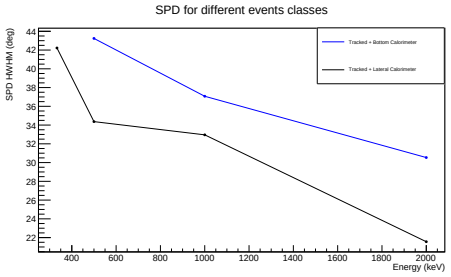

(d) SPD HWHM.

Figure B.1: Parameters estimated for the configuration with 20 layers.

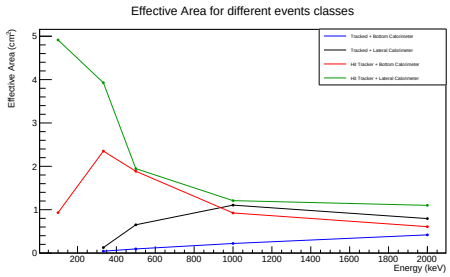

(a) Effective area.

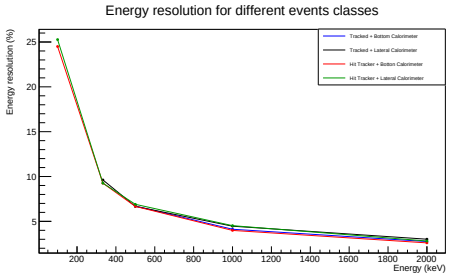

(b) Energy resolution.

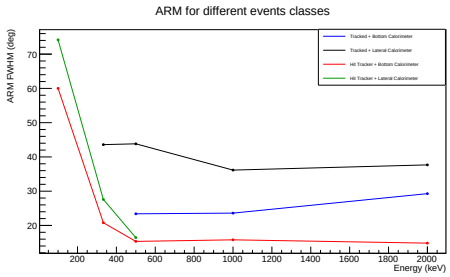

(c) ARM FWHM.

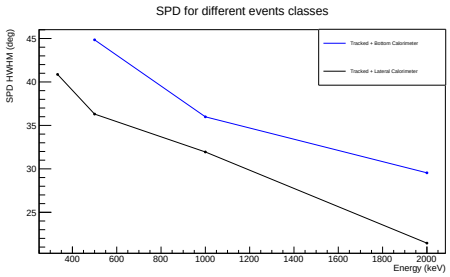

(d) SPD HWHM.

Figure B.2: Parameters estimated for the configuration with 25 layers.

Layers thickness simulations

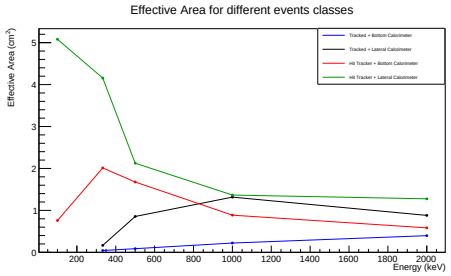

(a) Effective area.

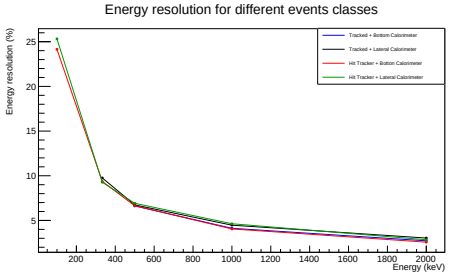

(b) Energy resolution.

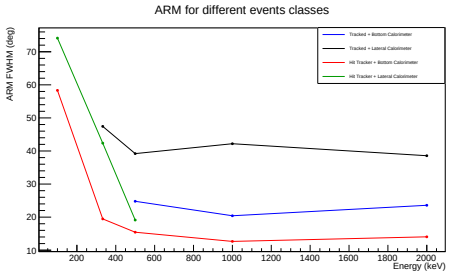

(c) ARM FWHM.

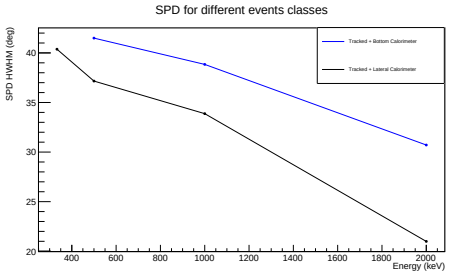

(d) SPD HWHM.

Figure B.3: Parameters estimated for the configuration with 400 μm layer thickness.

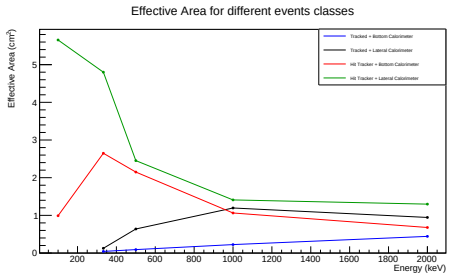

(a) Effective area.

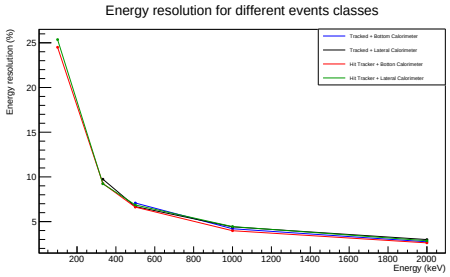

(b) Energy resolution.

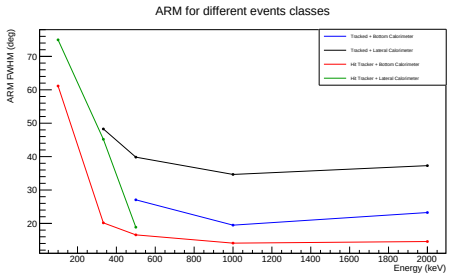

(c) ARM FWHM.

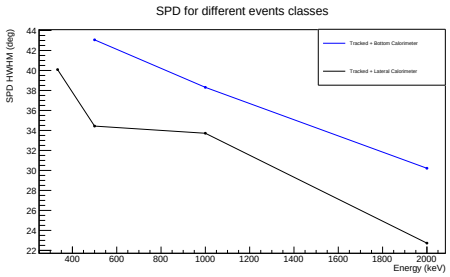

(d) SPD HWHM.

Figure B.4: Parameters estimated for the configuration with 600 μm layer thickness.

Strip pitch simulations

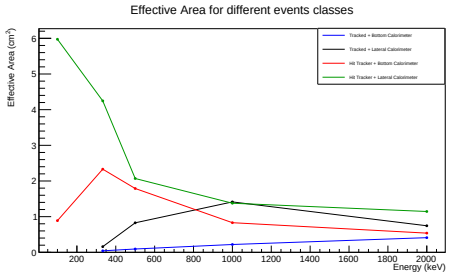

(a) Effective area.

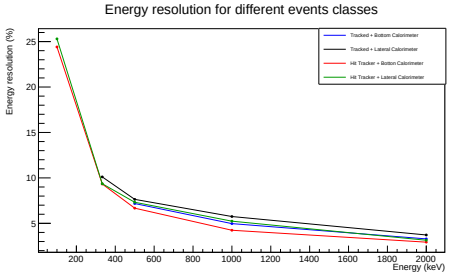

(b) Energy resolution.

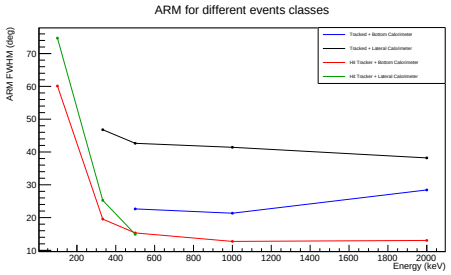

(c) ARM FWHM.

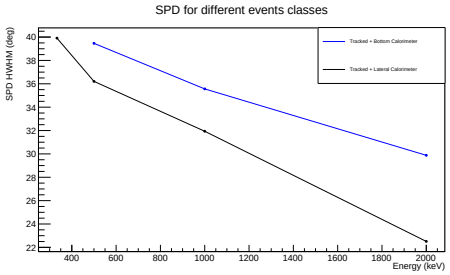

(d) SPD HWHM.

Figure B.5: Parameters estimated for the configuration with a strip pitch of 50 μm.

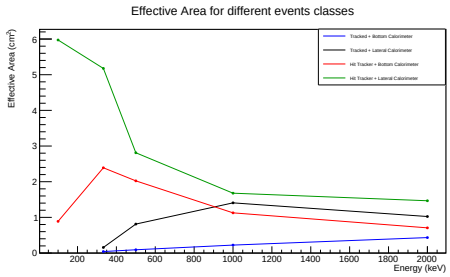

(a) Effective area.

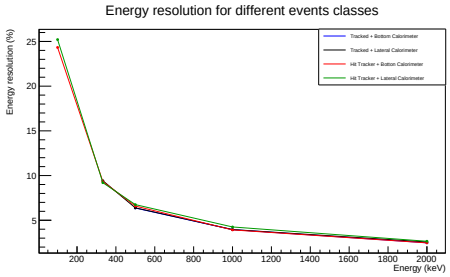

(b) Energy resolution.

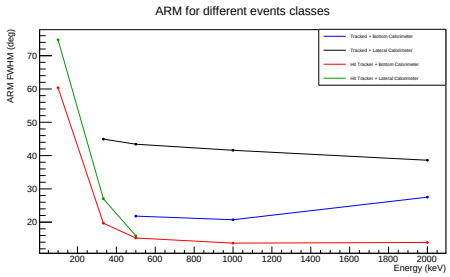

(c) ARM FWHM.

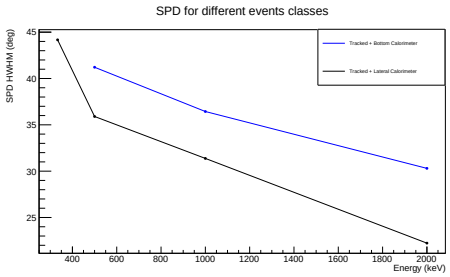

(d) SPD HWHM.

Figure B.6: Parameters estimated for the configuration with a strip pitch of 300 μm.

Bit digitization simulations

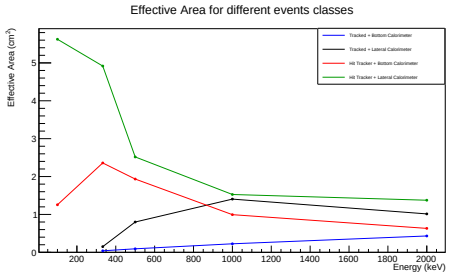

(a) Effective area.

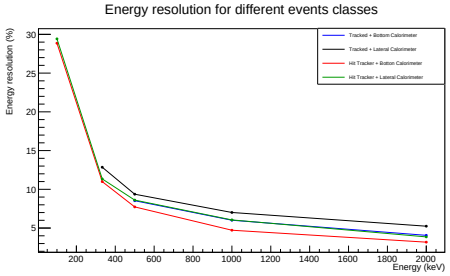

(b) Energy resolution.

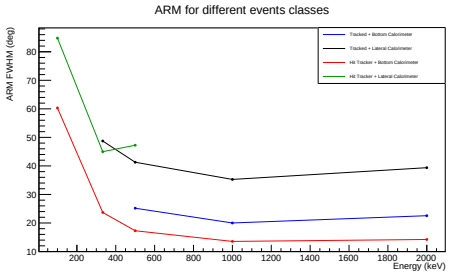

(c) ARM FWHM.

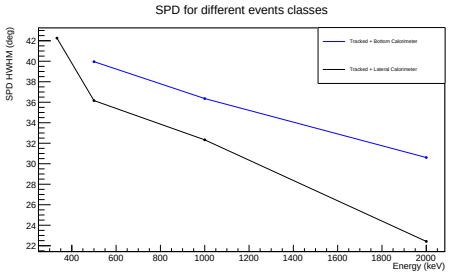

(d) SPD HWHM.

Figure B.7: Parameters estimated for the configuration with a 8 bit digitization.

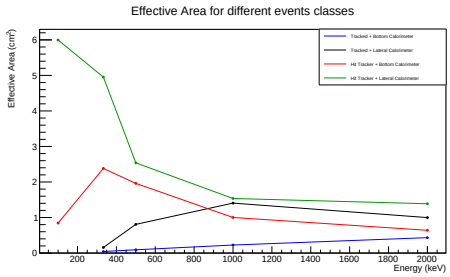

(a) Effective area.

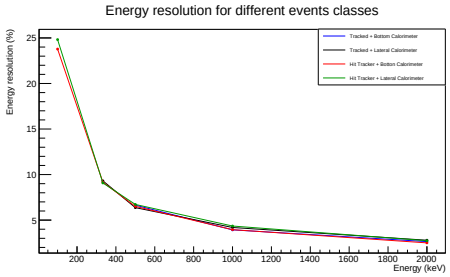

(b) Energy resolution.

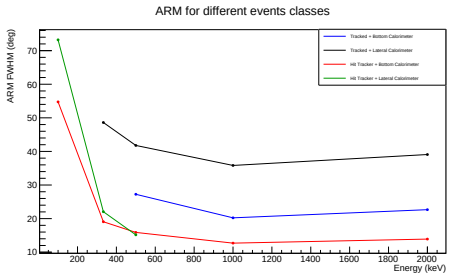

(c) ARM FWHM.

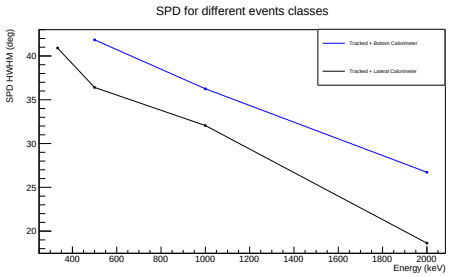

(d) SPD HWHM.

Figure B.8: Parameters estimated for the configuration with a 12 bit digitization.

Equivalent Noise Charge simulations

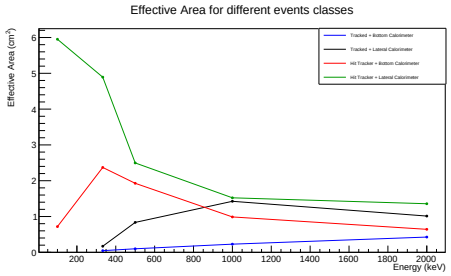

(a) Effective area.

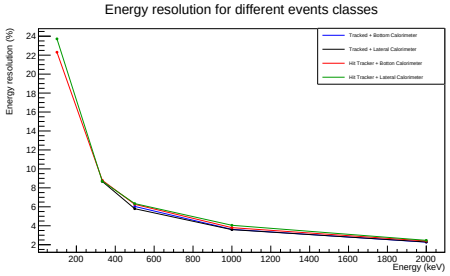

(b) Energy resolution.

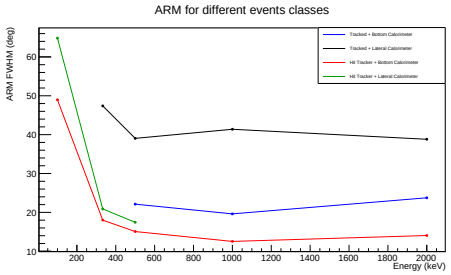

(c) ARM FWHM.

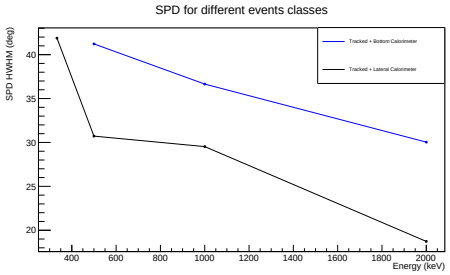

(d) SPD HWHM.

Figure B.9: Parameters estimated for the configuration with a 600 e^- ENC.

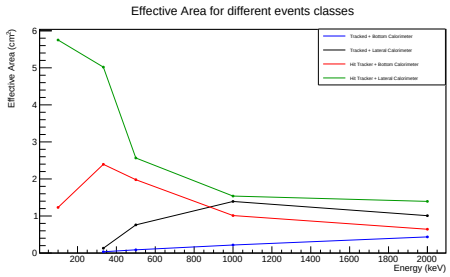

(a) Effective area.

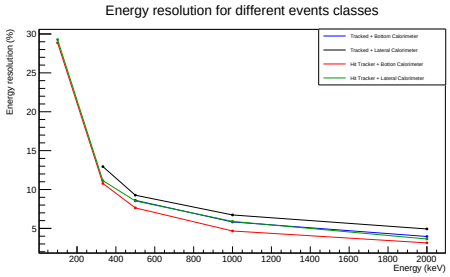

(b) Energy resolution.

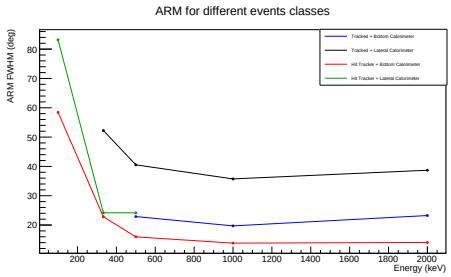

(c) ARM FWHM.

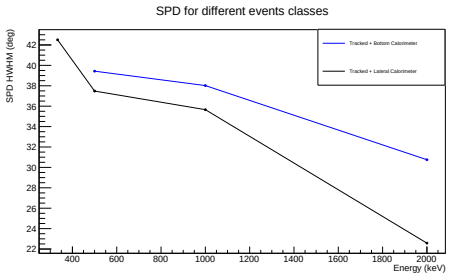

(d) SPD HWHM.

Figure B.10: Parameters estimated for the configuration with a 2400 e^- ENC.

Appendix C

Abbreviations and notations used

Abbreviations

SN	Supernova
GRB	Gamma-ray Burst
AGN	Active Galactic Nucleus
SED	Spectral Energy Distribution
ENC	Equivalent Noise Charge
ARM	Angular Resolution Measurement
SPD	Scatter Plane Deviation
PSF	Point Spread Function
EGB	Extragalactic Gamma-ray Background

Notations

E_i	Energy of the incident gamma-ray
E_e	Energy of the recoil electron
E_g	Energy of the scattered gamma-ray
φ	Compton scatter angle of gamma-ray
ε	Scatter angle of the recoil electron
ϑ	Total scatter angle
$\vec{e}_i$	Direction of the incident gamma-ray
$\vec{e}_e$	Direction of the recoil electron
$\vec{e}_g$	Direction of the scattered gamma-ray

F_z	Sensitivity
A_{eff}	Effective Area
T_{eff}	Observation time

Ringraziamenti

Sono molte le persone che vorrei ringraziare per aver reso possibile il completamento di questo lavoro. Innanzitutto, ringrazio il Dottor Riccardo Rando e il Professor Denis Bastieri per la disponibilità e per la pazienza dimostrata, per gli spunti e i consigli forniti, non solo nel corso di questo lavoro di Tesi Magistrale, ma anche in quello di Tesi Triennale. Ringrazio poi Francesco Berlato, con cui ho callaborato all'interno di questo progetto, e con il quale ho condiviso opinioni, dubbi e molti segmentation faults.
Ovviamente, i ringraziamenti devono essere estesi anche a tutte quelle persone che mi hanno aiutato nell'intero arco del percorso universitario e oltre. Innanzitutto alla mia famiglia, soprattutto a mia madre, che mi ha sempre sostenuto. Ringrazio poi tutti gli amici e colleghi Nicolò, Marco, Chiara, Daniele, Piero e Alessandro, con i quali ho condiviso lo stress e l'ansia per molti esami (anche se sarebbe meglio dire: che hanno sopportato il mio stress e la mia ansia), ma anche aperitivi molesti, serate nerd, canzoni trash e molti altri bei e petalosi momenti. Infatti, come disse una volta un "valoroso combattente": "Ragazzi, sono dei vostri!".

Bibliography

[1] F. Berlato. "Design and optimization around 1 MeV of a calorimeter for a CubeSat Mission". Master Thesis. Università degli Studi di Padova, 2016.

[2] M. Böettcher. "Modeling the emission processes in blazars". In: *Astrophysics and Space Science* 309 (2007).

[3] R. Diehl. "The COMPTEL experiment on the NASA Gamma-ray Observatory". In: *Space Science Reviews* 49 (1988).

[4] A. A. Abdo et al. "Fermi-LAT Observations of Markarian 421: the Missing Piece of its Spectral Energy Distribution". In: *The Astrophysical Journal* 736(2) (2011).

[5] A. C. Zoglauer et al. "Cosima – the Cosmic Simulator of MEGAlib". In: *IEEE Nuclear Science Symposium conference record. Nuclear Science Symposium* (2009).

[6] A. C. Zoglauer et al. "MEGAlib-Simulation and Data Analysis for Low-to-medium-energy Gamma-ray Telescopes". In: *Proceedings of the SPIE* 7011 (2008).

[7] A. C. Zoglauer et al. "MEGAlib — The Medium Energy Gamma-ray Astronomy Library". In: *New Astronomy Reviews 50(7)* (2006).

[8] A. Hoecker et al. "TMVA 4: Toolkit for Multivariate Data Analysis with ROOT, Users Guide". In: *arXiv:physics/0703039* (2013).

[9] A.A. Moiseev et al. "Compton-Pair Production Space Telescope (ComPair) for MeV Gamma-ray Astronomy". In: *arXiv:1508.07349* (2015).

[10] H. Odaka et al. "High-resolution Compton cameras based on Si/CdTe double-sided strip detectors". In: *Nuclear Instruments and Methods in Physics Research, section A* (2012).

[11] M. Böettcher et al. "Leptonic and Hadronic Modeling of Fermi-Detected Blazars". In: *The Astrophysical Journal* 768 (2013).

[12] P. A. Milne et al. “Supernova Science with an Advanced Compton Telescope”. In: *arXiv:astro-ph/0012078* (2000).

[13] P. Bloser et al. “Development of Silicon Strip Detectors for a Medium Energy Gamma-ray Telescope”. In: *arXiv:astro-ph/0302500* (2003).

[14] S. Boggs et al. “Advanced Compton Telescope (ACT): witness to the fires of creation”. Proposal. 2005.

[15] V. Schönfelder et al. “Instrument description and performance of the Imaging Gamma-Ray Telescope COMPTEL aboard the Compton Gamma-Ray Observatory”. In: *Astrophysical Journal Supplement Series* 86 (1993).

[16] W. B. Atwood et al. “The Large Area Telescope on the Fermi Gamma-ray Space Telescope Mission”. In: *The Astrophysical Journal* 697 (2) (2009).

[17] ideas ASA, ed. *VA64TA1 datasheet*. 2004.

[18] S. Cheenu Kappadath. “Measurement of the Cosmic Diffuse Gamma-Ray Spectrum from 800 keV to 30 MeV”. PhD Thesis. University of New Hampshire, 1998.

[19] R. Marc Kippen. “The GEANT Low Energy Compton Scattering (GLECS) Package for use in Simulating Advanced Compton Telescopes”. In: *New Astronomy Reviews* 48 (2004).

[20] Glenn F. Knoll. *Radiation Detection and Measurement*. Ed. by John Wiley and Sons Inc. 2010.

[21] V. Schönfelder. “Lessons learnt from COMPTEL for Future Telescopes”. In: *New Astronomy Reviews* (2003).

[22] V. Schönfelder and G. Kanbach. “Imaging through Compton scattering and pair creation”. In: *Observing Photons in Space: a guide to Experimental Space Astronomy* (2013).

[23] Helmuth Spieler. *Semiconductor Detector Systems*. Ed. by Oxford University Press. 2005.

[24] H. Tajima. *Front-end Card Specification for VA64TA*. 2007.

[25] M. Tavani and V. Tatischeff. “ASTROGAM: Proposal for the ESA M4 Mission Programme”. Proposal. 2015.

[26] C. M. Urry and P. Padovani. “Unified Schemes for Radio-Loud Active Galactic Nuclei”. In: *Astronomical Society of the Pacific* 715 (1995).

[27] M. Tavani V. Tatischeff. "The e-ASTROGAM gamma-ray space mission". In: *Proc. SPIE 9905, Space Telescopes and Instrumentation 2016: Ultraviolat to Gamma Ray* (2016).

[28] H. Voss. "Data Analysis with TMVA". In: *Seminar, Lausanne* (2010).

[29] A. C. Zoglauer. *Cosima, a Cosmic Simulator for MEGAlib based on Geant4*. 2015.

[30] A. C. Zoglauer. "First Light for the Next Generation of Compton and Pair Telescopes". PhD Thesis. Max Planck Institut für Extraterrestrische Physik, 2005.

[31] A. C. Zoglauer. *Geomega, Geometry for MEGAlib*. 2014.

[32] A. C. Zoglauer. *Mimrec, MEGAlib image reconstruction and more ...* 2010.

[33] A. C. Zoglauer. *The MEGAlib software package*. 2006.